J. Fluid Mech. (2024), *vol*. 989, A16, doi:10.1017/jfm.2024.518

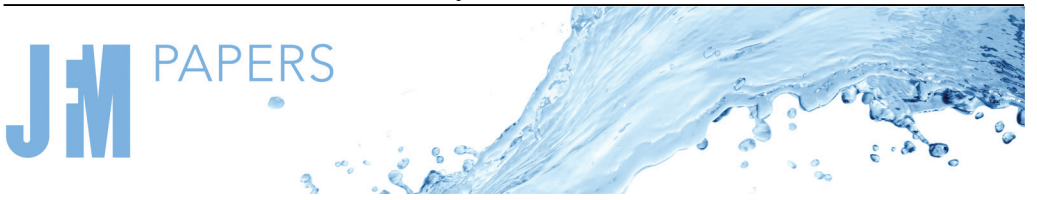

Variability of convection velocities and structure inclination angles in wall-bounded turbulence

G. Cui[1] **and I. Jacobi**[1],†

[1]Faculty of Aerospace Engineering, Technion Israel Institute of Technology, Haifa 32000, Israel

(Received 14 January 2024; revised 20 May 2024; accepted 21 May 2024)

The scale-dependent variability of convective velocities and structure inclination angles in wall-bounded turbulence was studied experimentally via space–time energy spectrum measurements. We found that the variability of convection velocities for large-scale motions (LSMs) decreased inversely with streamwise wavenumbers, and that the variability trend was not fully explained by earlier applications of Kraichnan's 'random-sweeping' model of turbulence that assumed perfect scale separation. By analytically extending the random-sweeping model to allow for a dominant large scale in the random-sweeping signal that can interact with other LSMs, we showed how scale interactions can explain the variability trend in convection velocities for LSMs. The variability in convection velocities was also shown to correlate with the scale-dependent inclination angles of coherent structures that were obtained via cross-spectral analysis. Large-scale motions tended to exhibit shallower inclination to the wall with increasing convection velocity, while small-scale motions and those far from the wall exhibited the reverse behaviour. We proposed that these two opposite relationships between inclination angle and convection velocity can be explained in terms of a balance between opposing effects of the mean shear and the coherent structure geometry. Descriptions and models of convection velocity variability effects are useful both for modelling turbulence spectra and explaining the geometry of coherent structures.

Key words: turbulent boundary layers, turbulence theory, boundary layer structure

1. Background

The problem of describing the scale-dependent convection velocities of coherent structures in wall-bounded turbulence has been important since the earliest questions about the validity of Taylor's frozen turbulence hypothesis. Most of this work has focused on

† Email address for correspondence: ijacobi@technion.ac.il

quantifying useful measures of the mean convection velocity as an alternative to Taylor's hypothesis, while comparatively less attention has been devoted toward describing the scale-dependent variation of the convection velocities about their mean. But understanding this variation has become important for developing models of the space–time turbulence spectrum and for understanding the structural differences between coherent motions moving at different velocities. The current study seeks to address both of these problems.

Lin (1953) first identified the conditions under which Taylor's froze turbulence hypothesis is expected to fail, particularly for large-scale coherent structures in highly anisotropic flows. Since then, efforts to describe the deviations from Taylor's hypothesis have broadly fallen into two categories: modelling the space–time correlations and spectra from which convection velocities can be predicted, and quantifying the convection velocities obtained from experiments and computational simulations.

1.1. *Models of the space–time spectrum of turbulence*

Kraichnan (1964) and Lumley (1965) both proposed a model spectrum of turbulence in which small-scale turbulent fluctuations, u, were convected by a spatially and temporally uniform fluctuating field, v, in addition to some mean velocity, U. Lumley found that the width of the resulting frequency spectrum, as measured by its normalized second moment, was described by the magnitude of fluctuations of the convective velocity, $\langle v^2 \rangle$, divided by their corresponding Taylor microscale. Therefore, the observed broadening of the energy spectrum was indicative of variations in instantaneous convection velocities about the mean convection velocity predicted by Taylor's hypothesis. Kraichnan utilized this same scalar convection model of turbulence to study the more general validity of Kolmogorov's assumption that large and small scales are statistically independent when sufficiently separated. Since Kraichnan's work, this convection model has been referred to as the 'random-sweeping hypothesis', since the large scale, v, was assumed to sweep the turbulence along as a passive scalar.

The random-sweeping model was extended by Wilczek & Narita (2012) to obtain an analytical expression for the frequency–wavenumber spectrum, in which the mean convection velocity was represented by Taylor's hypothesis and the width of the spectrum in the frequency domain was found to scale with the magnitude of fluctuations of the convective velocity, $\langle v^2 \rangle$, consistent with Lumley. They also showed that their model was consistent with predictions from an alternative, elliptic approximation model (He & Zhang 2006; He, Jin & Yang 2017). Wilczek, Stevens & Meneveau (2015*b*) later applied this analytical spectral model to the case of wall-bounded flows by using the Townsend's log law for the Reynolds stresses to represent the turbulence intensity associated with the spectral width (Marusic *et al.* 2013). They reported good qualitative agreement between the analytical frequency–wavenumber spectrum and that obtained via large eddy simulations (LES), although some deviations were apparent.

Importantly, Wilczek *et al.* (2014) noted that the true spectral width (in the frequency domain) is non-zero when approaching the smallest wavenumbers, and yet the one-dimensional (1-D) random-sweeping model predicted zero width in this limit. They attributed this discrepancy to two possible sources: the neglect of scale interactions at the large scales of turbulence and the lack of influence from spanwise wavenumbers. Later, Wilczek, Stevens & Meneveau (2015*a*) extended the 1-D sweeping model to include spanwise wavenumbers and showed how this appeared to resolve the low-wavenumber singularity, but they did not provide a quantitative comparison of spectral width variation with wavenumbers, and they left open the question of the influence of scale interactions.

Liu & Gayme (2020) proposed an alternative approach to calculating the distribution of convection velocities based on a linearized, input–output model of turbulent channel flow, and they estimated power-spectral densities as a function of convection velocity, where the width of the power spectrum was shown to narrow for smaller scales and was found to be roughly symmetric about the mean convection velocity (except for certain intermediate-sized scales), largely consistent with the sweeping model predictions. However, they also did not report quantitative comparisons of spectral width with respect to wavenumber, and their linear analysis necessarily neglected the influence of scale interactions.

There are a number of analytical tools available for describing and reconstructing the width of the space–time spectrum, most of which appear in the important study by Beall, Kim & Powers (1982). If we denote the turbulent spectral density of the streamwise velocity component, u, with streamwise wavenumber, k_x, and frequency, ω, as $\phi_{uu}(k_x, \omega)$, then Beall *et al.* (1982) introduced the idea of a 'conditional spectral density', $\phi_{uu}(\omega|k_x)$, as the normalized spectrum

$$\phi_{uu}(\omega|k_x) = \frac{\phi_{uu}(k_x, \omega)}{\int_{-\infty}^{\infty} \phi_{uu}(k_x, \omega)\,\mathrm{d}\omega}, \tag{1.1}$$

such that $\phi_{uu}(\omega|k_x)\Delta\omega$ represents the fraction of power at k_x due to fluctuations between $(\omega, \omega + \Delta\omega)$ and is analogous to a conditional probability. This means that the conditional spectral density can be interpreted naturally as a probability density function (p.d.f.), and according to the model of Wilczek & Narita (2012), that p.d.f. is predicted to be a normal distribution. (The results of Liu & Gayme (2020) show some non-Gaussian spectral distributions for intermediate k_x scales, but Wilczek *et al.* (2015*a*) found that the Gaussian behaviour was largely maintained even for anisotropic, wall-bounded flows.) As a consequence, the conditional spectral density can be used directly to determine the spectral width by integrating its second moment (variance) directly, as discussed in Narita (2017).

Because the spectral width in the frequency domain, ω, can be transformed into a spectral width in the phase-speed domain, c, for a fixed wavenumber, where $c = \omega/k_x$, the spectral width provides a direct measure of the variability of the turbulent energy across phase speeds, which is a natural way of thinking about the sweeping model described above, where the variance of the analytical spectrum was found to depend on the variance of the large-scale velocity signal, $\langle v^2 \rangle$.

In addition to the direct measurement of the spectral moments from the space–time spectrum, Beall *et al.* (1982) also showed that the spectral moments can be inferred from the joint p.d.f. of the auto-spectral energy and local frequencies (or wavenumbers) that are defined via the cross-spectrum. This technique allows for the reconstruction of the space–time spectrum with limited two-point measurements in either one of the dimensions, a technique that was later employed by De Kat & Ganapathisubramani (2015). Furthermore, Beall *et al.* (1982) showed that the spectral variance calculated from the joint p.d.f. is expected to differ from the direct integration of the spectral moment by an amplitude-dependent term – this result was later emphasized by Wu *et al.* (2017) who empirically compensated for the discrepancy in their spectral models (see their review of these topics in Wu & He 2021*a*). However, all of these techniques for quantifying the spectral width must be applied with care, in particular, accounting for the limitations of experiments, which have mostly focused on establishing a mean convection velocity and not its variance.

1.2. *Measurement and quantification of convection velocities*

A significant number of experimental studies have sought to measure the mean convection velocities of coherent structures in turbulence, from the early studies of Cliff & Sandborn (1973) and later Kim & Hussain (1992), to more recent efforts to measure the space–time spectrum directly with particle image velocimetry (PIV) by Dennis & Nickels (2008), Elsinga *et al.* (2012) and LeHew, Guala & McKeon (2011). The key computational study by Del Álamo & Jiménez (2009) summarized many of the challenges in defining a single characteristic convection velocity for each wavenumber or frequency, given the width of the space–time spectrum in both dimensions, and they proposed weighted-integral approaches to answer this question consistently. Some physical insights into this problem from a transport perspective were later offered by Geng *et al.* (2015). A comprehensive study of the convection velocity, based on an LES calculation at $Re_\theta = 13\,000$ was performed by Renard & Deck (2015), who also reviewed and tabulated all the previous measurements and calculation techniques.

Despite the extensive studies involving wavenumber–frequency spectra, there are very few reports of the wavenumber dependence of the frequency spectrum variance. Direct numerical simulation (DNS) channel flow calculations of the spectral variance at $Re_\tau = 187$ (Yang *et al.* 2020) and $Re_\tau = 550$ (Wu & He 2021*b*) have been reported, although they enforced Taylor's hypothesis in their definition of the second spectral moment, and their Reynolds numbers were relatively low.

1.3. *Convection velocities and the inclination angles of coherent structures*

Like the interest in the scale dependence of convection velocities, there has been similar interest in the scale dependence of coherent structure inclination angles. Deshpande, Monty & Marusic (2019) reported inclination angle variation as a function of streamwise wavelength for different spanwise scale sizes, and validated the traditionally assumed inclination angle of 45° for individual, large-scale, wall-attached structures (as opposed to the 15° for overall packets). Li *et al.* (2022) examined the same scale dependence of inclination angles in the atmospheric surface layer under both unstable and neutrally stable conditions. Following Chauhan *et al.* (2013), they developed a log-law-type empirical formula to relate the inclination angle and structure wavelength.

A few studies have looked at how structure geometry and scale-specific convection velocity are related. LeHew, Guala & McKeon (2013) examined the connection between the convection velocity of vortices and whether they were attached to the wall and found a higher variance in the convection velocity for attached structures. Lozano-Durán & Jiménez (2014) performed a similar analysis, computationally. More recently, Huang (2019) developed a model to relate the mean velocity profile to the inclination angles of coherent structures by utilizing an expression for the variance of velocity fluctuations for an individual eddy by Banerjee & Katul (2013). They confirmed that the inclination angle can be used to improve predictions of the mean velocity profile, via comparison with DNS profiles, although they did not explore the indirect dependence of their model on the local convection velocity variance, which would require detailed measurements of the local, scale-dependent convection velocities of the eddies. The relationship between scale-specific convection velocity and inclination angle of coherent structures also arises in the context of resolvent-based modelling of turbulence, in which the phase velocity of modes dictates the mode shape, including its relative inclination to the wall (see McKeon (2017) for an overview and Cui & Jacobi (2023) for specific observations on inclination angles).

In this study we performed experimental measurements of a turbulent boundary layer to obtain the scale-dependent variance of phase speeds and to examine its relationship to the scale-dependent inclination angles of coherent structures in the flow. The experiments are described in § 2. In § 3 we report the spectral variance of phase speed as a function of streamwise and spanwise wavenumbers and identify persistent discrepancies with previous versions of the random-sweeping model. We extend the random-sweeping model of turbulence (under simplifying assumptions) to include 1-D scale interactions in order to explain the dominant streamwise-wavenumber dependence of variance for large-scale motions (LSMs). Then, in § 4 we explore the relations between structure size, inclination angle and phase speed, using space–time cross-spectral analysis, in order to develop intuition about how variations in phase speed are associated with the average inclination angles of velocity modes, the size of the modes and the strength of the mean shear of the flow field.

2. Turbulent boundary layer experiments and validation

Measurements of a zero-pressure gradient turbulent boundary layer were performed along the bottom wall of a high-speed water tunnel facility with a test section of length 2000 mm and a cross-section 200 × 200 mm. The flow was tripped with a 1 mm trip wire at the inlet to the test section, and two-dimensional (2-D), time-resolved, planar PIV measurements were recorded in the streamwise/wall-normal (x/y) and wall-parallel (x/z) planes starting 1160 mm downstream of the trip. More details about the water tunnel and PIV experiment in the tunnel can be found in Cui, Ruhman & Jacobi (2022).

Five different free-stream velocities, U_∞, in the range $0.52\,\mathrm{m\,s^{-1}}$ to $3.76\,\mathrm{m\,s^{-1}}$ were considered in the streamwise/wall-normal experiments to cover the low and moderate range of $Re_\tau = u_\tau \delta/\nu$ ranging from 530 to 3070, where u_τ is the friction velocity, δ is the boundary layer thickness based on δ_{99} and ν is the kinematic viscosity. The wall-parallel experiment was performed at $Re_\tau = 3070$ only, at a wall location of 3 mm, corresponding to the middle of the log layer at $y/\delta = 0.13$ and $y^+ = 400$. The streamwise field of view (FOV) extended for $>15\delta$ for all cases and was imaged with two high-speed cameras (Phantom VEO-340L and VEO-440L) operating at a spatial resolution of 2560 × 440 pixels each, recording at 1.5 kHz for the wall-normal measurements and 2560 × 800 pixels and 0.8 kHz for the wall-parallel case. The flow was seeded with 10 µm glass particles with a density of $1.1\,\mathrm{g\,cm^{-3}}$ and illuminated with a high-speed laser (Litron 527). The laser was operated in single-pulsed mode for the lowest-Reynolds-number case, and double-pulsed mode for the higher-Reynolds-number cases due to limitations on the recording frequency of the cameras. For each Reynolds number, ten recordings were made to accumulate at least 1000 eddy turnover times worth of temporal data (40 recordings for the wall-parallel case). The velocity vectors were calculated using commercial software (Davis 10.2.1). The multipass vector calculation includes two passes: a square 32 × 32 pixel interrogation window, followed by a 16 × 16 pixel circular window, using 50 % in both cases to avoid spatial aliasing (LeHew 2012). Details about the flow and resolution for each case are summarized in table 1. The PIV was not fully resolved in time or space for the smallest-scale features at higher Reynolds numbers, but the analysis will focus primarily on large-scale features.

Figure 1(*a*,*b*) shows the mean velocity profiles and the streamwise normal Reynolds stresses for all five Reynolds numbers compared with the canonical data by Fernholz & Finley (1996) at similar Re_τ. For the lowest Reynolds number, both the mean velocity profile and the turbulent intensity match very well, whereas the normal Reynolds stress

U_∞ (m s^{-1})	δ (mm)	θ (mm)	Re_τ	Re_θ	u_τ (m s^{-1})	L_x/δ	Δx^+	Δt (μs)	Δt^+	T_E
0.52	23.6	2.5	530	1210	0.024	15.5	19.6	500	0.27	1210
1.21	22.9	2.5	1080	2830	0.050	16.0	41.1	678	1.60	1970
2.02	22.4	2.3	1690	4460	0.080	16.4	65.7	678	4.08	3360
2.85	23.6	2.5	2410	6660	0.108	15.5	89.2	678	7.52	4480
3.76	23.3	2.4	3070	8730	0.140	15.8	115.2	678	12.53	6010
3.76	23.3	2.4	3070	8730	0.140	15.0	76.1	1250	23.5	23 870

Table 1. Statistical features of the five different streamwise/wall-normal experiments, followed by the wall-parallel experiment (below the line): free-stream velocity, U_∞; boundary layer thickness, δ defined as δ_{99}; momentum thickness, θ; friction Reynolds number, Re_τ; friction velocity, u_τ; streamwise field view, L_x; spatial resolution (inner units), Δx^+; temporal resolution (inner units), Δt^+; record length in eddy turnover times, T_E. The spanwise extent for the wall-parallel experiment was $L_z/\delta = 2.4$.

becomes attenuated with increasing Re_τ as expected, due to the resolution limits of the PIV window (Foucaut, Carlier & Stanislas 2004; LeHew *et al.* 2011).

Figure 1(*c*,*d*) shows the premultiplied 1-D spatial spectral densities of the streamwise turbulent fluctuations with respect to the streamwise wavenumber, k_x, compared with spectra reported from channel flow DNS at comparable Re_τ. As with the normal Reynolds stress, the spectral density compares well at low Re_τ (figure 1*c*) but shows the increasing effect of attenuation at high Re_τ (figure 1*d*). Foucaut *et al.* (2004) reported that the spectral attenuation due to PIV becomes significant (i.e. more than 50 % attenuation) above a wavenumber cutoff $k_{cut} = 2.8/W$, where $W = 2\Delta x$ is the PIV window size (with 50 % overlap). This cutoff wavenumber is marked in the red dashed lines, and compares well with the actual point of 50 % attenuation from the current experiments marked in black dashed lines. All of the subsequent analysis will focus on wavenumbers below this threshold.

3. Scale-dependent variance of convection velocities

3.1. *Space–time spectral density*

The 2-D space–time spectral energy density with respect to streamwise wavenumber, k_x, and frequency, ω, was calculated from the 2-D fast Fourier transform (FFT) of the fluctuating velocity for each height from the streamwise/wall-normal measurements. Each of the continuous time series was segmented by Welch's method with a temporal segment size selected to be comparable to the spatial domain size of the FOV. The mean was removed and Hanning windows were applied to both the streamwise spatial and temporal segments. The data was zero padded, and the FFT was calculated with 50 % overlap between the segments, all following the procedure in LeHew *et al.* (2011) with the exception of mean removal, where they removed the global mean and we removed the segment mean. The effect of the choice of mean removal on the energy of LSMs is explored in detail in Appendix A.

The k_x/ω spectrum is shown in figure 2(*a*), where the slope of the solid red line indicates the convective velocity associated with Taylor's hypothesis and the dashed cyan line indicates the frequency-weighted average velocity obtained from the first spectral moment (Jiménez, Del Alamo & Flores 2004; Flores & Jimenez 2006). The black contour line marks the isocontour of spectral energy density that contains within it 30 % of the total

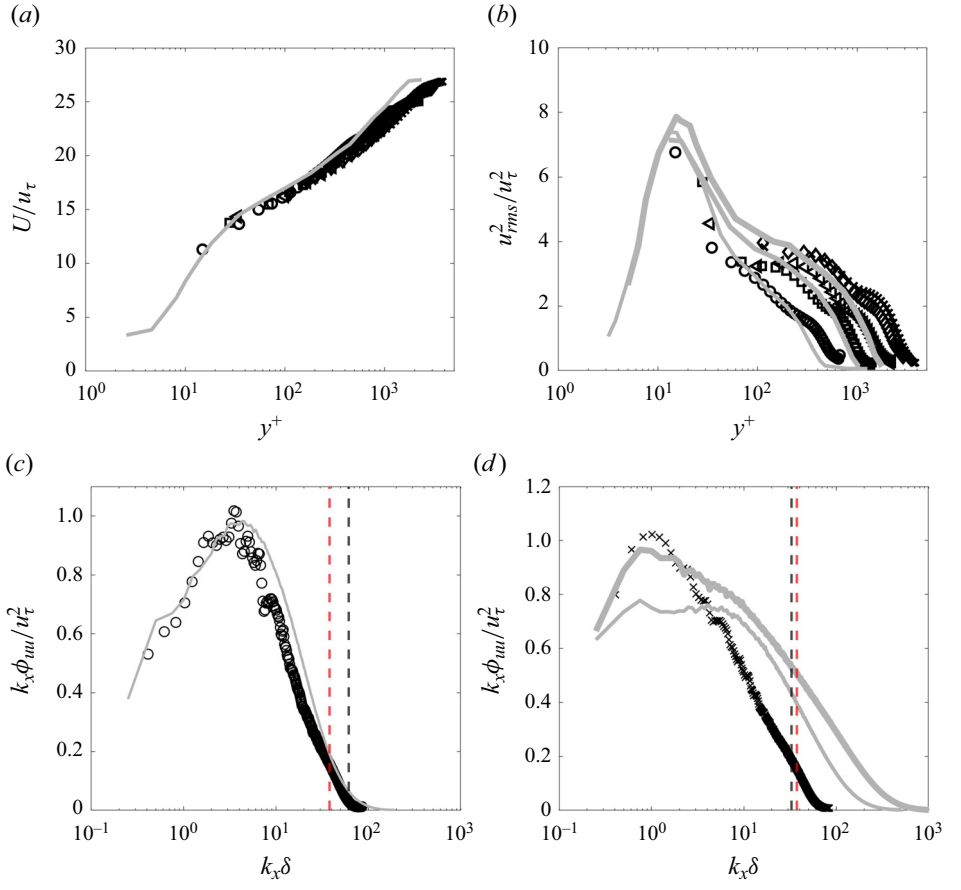

Figure 1. (*a*) Mean streamwise velocity profiles for all five Re_τ (black symbols: $Re_\theta = 1210$ circle; $= 2830$ square; $= 4460$ triangle; 6660 diamond; 8730 cross) compared with measurements by Fernholz & Finley (1996) at $Re_\theta = 5023$ (grey line). (*b*) Streamwise normal Reynolds stress profiles compared with Fernholz & Finley (1996) at $Re_\theta = 1208, 2777, 4736$ (grey lines, thickness increasing with Re_θ). (*c*) Premultiplied, spatial energy density measured at $y/\delta \approx 0.1$ for the lowest Reynolds number $Re_\tau = 530$ (black circles) compared with DNS channel flow data at $Re_\tau = 550$ (Del Álamo *et al.* 2004) (grey line). (*d*) Premultiplied energy spectral density for the highest Reynolds number $Re_\tau = 3070$ (black crosses) compared with DNS channel flow data at $Re_\tau = 2000$ (Hoyas & Jiménez 2006) and 5200 (Lee & Moser 2015) (grey lines, thickness increasing with Re_τ). The vertical dashed lines represent the wavenumbers at which the PIV spectral energy density is attenuated by 50 % compared with the DNS (black line is experimental, red line corresponds to the empirical result from Foucaut *et al.* 2004).

streamwise turbulent kinetic energy (TKE), $\overline{u'^2}$. This constant energy fraction contour was used to observe trends in the spectral distribution of the streamwise TKE as a function of wall-normal height, shown in figure 2(*b*) and as a function of Reynolds number, shown in figure 2(*c*). For validation, the space–time spectral density from the wall-parallel plane at this height (not shown), integrated over all spanwise wavenumbers, k_z, was found to match the spectrum obtained from the streamwise/wall-normal measurements.

As the wall-normal position increases, the energy fraction contour expands to include more small-scale, high frequency content (beyond the wall-normal location of the outer LSM peak). The large-scale, low frequency region of the contour also shifts slightly to larger, faster coherent motions appearing further away from the wall. For a

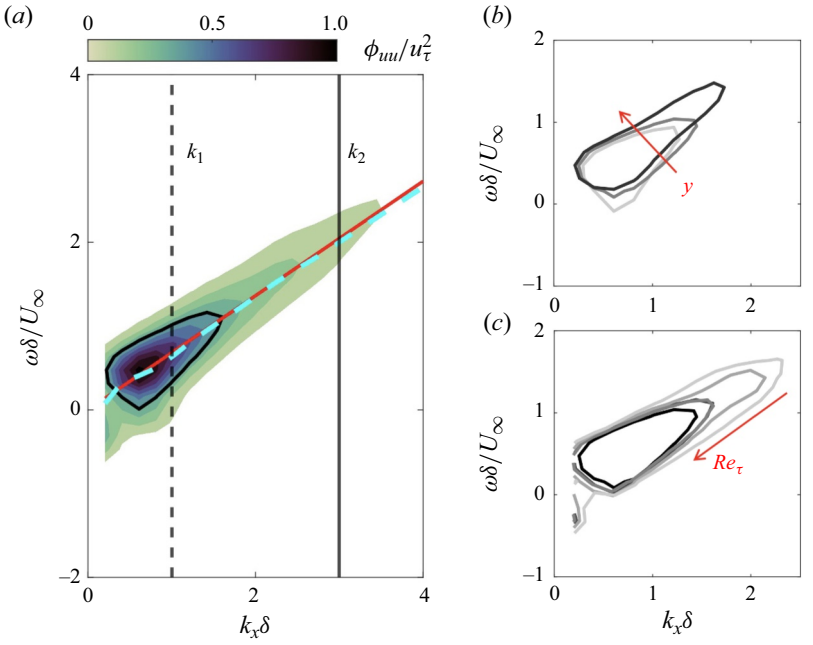

Figure 2. (*a*) Space–time spectral energy density, $\phi_{uu}(k_x, \omega)$ at $y/\delta \approx 0.1$ for $Re_\tau = 3070$. The local mean velocity (Taylor's hypothesis) is marked in red; the average convection velocity (Jiménez *et al.* 2004) is marked in dashed cyan. The isocontour of spectral energy containing 30 % of the streamwise TKE is in black. (*b*) The 30 % energy fraction contours for varying wall-normal locations, $y/\delta \approx 0.04, 0.1, 0.5$ (darker lines at higher y), at fixed $Re_\tau = 3070$. (*c*) The energy fraction contours for varying Re_τ (darker lines at higher Re_τ) at $y/\delta \approx 0.1$.

fixed wall-normal location (in outer units), increasing the Reynolds number results in a contraction of the energy contour, indicating increased domination of the flow by large-scale coherent motions. But ultimately, the Reynolds numbers effects on the large scales are rather weak over this range, as noted in the subsequent analysis.

Previous studies (Jiménez *et al.* 2004; Flores & Jimenez 2006; LeHew *et al.* 2011) have focused on the fact that the weighted-average convective velocity, marked as the cyan line in figure 2(*a*), does not have a constant slope, as Taylor's hypothesis would dictate (red line), but varies with wavenumber, with the greatest deviation for the large scales near the wall. However, in addition to the variation of the weighted average frequency with wavenumber, figure 2(*a*) also shows a significant variation in the width of the frequency spectrum with wavenumber. The width of the frequency spectrum for a given wavenumber can be thought of in terms of the phase velocity variation, since $c = \omega/k_x$, and thus represents the distribution of energy across different phase velocities associated with velocity modes of that particular wavenumber. Based on this, variations in the width of the space–time spectrum with wavenumber indicate that the distribution of convective velocities is strongly size dependent. However, from figure 2(*b*,*c*), it is clear that the distribution of convective velocities (the width of the ω-spectral density) varies only weakly with wall-normal location, y, and Re_τ. However, stronger y variation is expected in the near wall region below the log layer that was not resolved in the experimental measurements.

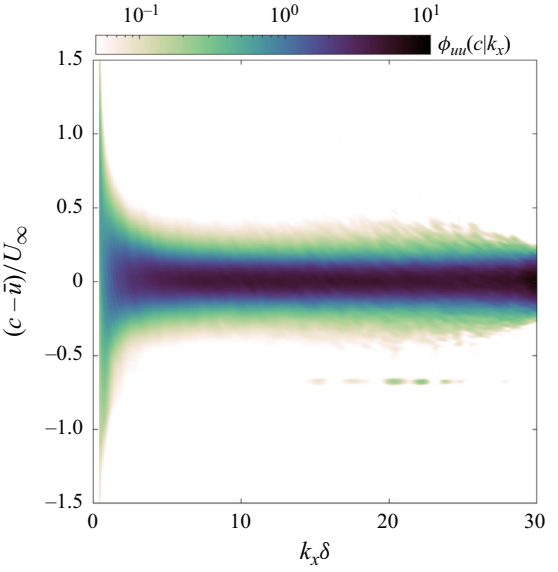

Figure 3. The conditional wavenumber spectrum, $\phi_{uu}(c|k_x)$, following Beall *et al.* (1982), but in terms of the deviation of the phase speed, c, from the local mean velocity, $\bar{u}$ dictated by Taylor's hypothesis. For $k_x\delta \gtrsim 25$, the SNR < 10 and the distribution tails are truncated.

3.2. *Conditional wavenumber spectrum and convection velocity variance*

In order to quantify the changing distribution of convective velocities with structure size, we first transform the frequency, ω, of the 2-D spectrum, $\phi_{uu}(k_x, \omega)$, into phase speed c, via the relation $c = \omega/k_x$, to obtain $\phi_{uu}(k_x, c)$. Then we employ the conditional wavenumber spectral density described by Beall *et al.* (1982) to calculate the p.d.f. of phase speeds for each wavenumber, $\phi_{uu}(c|k_x)$. The conditional spectrum provides a spectral view on the relative distribution of phase speeds associated with the coherent structures in the boundary layer. The distribution of phase speeds is here taken as representative of the distribution of convective velocities, and the terms will be used interchangeably, forgiving the slight imprecision involved. Similarly, the mode shapes associated with individual wavenumbers are assumed to characterize the typical coherent structure of the corresponding scale, although in reality coherent structures contain spectral energy content from a range of wavenumbers.

For calculating conditional spectral density, it is important to remove the noise floor of the spectrum due to the PIV measurements first, in order not to contaminate the shape of the resulting p.d.f. by the appearance of spurious distribution tails that are actually just noise. This baseline subtraction was based on the power calculated at the Nyquist frequency, following Oxlade *et al.* (2012). The resulting conditional spectrum is shown in figure 3. The wavenumber dependence of the width of the convective velocity distribution is quite prominent, particularly for the large scales, $k_x\delta \lesssim 2\pi$. Past a wavenumber of $k_x\delta \gtrsim 25$, the signal-to-noise (SNR) ratio – defined as the ratio between the spectral peak and noise floor – dips below 10. Thus, the noise floor becomes so large relative to the turbulent spectral energy that the distribution becomes noticeably truncated for these high wavenumbers.

The predicted shape of the conditional spectrum $\phi_{uu}(c|k_x)$ was obtained by Wilczek & Narita (2012), based on the random-sweeping model of Kraichnan (1964). As noted in the

introduction, the sweeping model assumes that a small-scale turbulence field, $u(x, t)$, is advected by a large-scale (sweeping) velocity field, v, and a background mean velocity, U, where the u and v are statistically independent due to scale separation. For notational simplicity, only the streamwise components and derivatives of the fields are described here. The streamwise linearized advection equation describing this system can be written as

$$\frac{\partial u}{\partial t} + (U + v)\frac{\partial}{\partial x}u = 0, \tag{3.1}$$

where $U + v$ represents the instantaneous velocity advecting the small-scale turbulence, u. Wilczek & Narita (2012) then developed a full space–time spectrum from this equation by transforming and solving it in wavenumber space, then constructing the two-point covariance tensor and finally transforming again to frequency space. In this procedure, the velocity $u(x, t)$ was assumed to vary in space and time, while v was assumed uniform in space and time, with Gaussian-distributed fluctuations across the ensemble. The uniformity of v represented a significant scale separation between the turbulence being advected and the large-scale fluctuations causing the advection. The final form of the space–time spectrum, $\phi_{uu}(k_x, \omega)$, took the form of normal distributions in the frequency domain for each wavenumber k_x, centred on the frequency $k_x U$ that is associated with Taylor's hypothesis:

$$\frac{\phi_{uu}(k_x, \omega)}{\phi_{uu}(k_x)} = \frac{1}{\sqrt{2\pi}}\frac{1}{\sqrt{k_x^2\langle v^2\rangle}}\exp\left[-\frac{1}{2}\frac{(\omega - k_x U)^2}{k_x^2\langle v^2\rangle}\right]. \tag{3.2}$$

Transforming this result from the frequency domain, ω, to the phase-speed domain, $c = \omega/k_x$, and writing in the form of the conditional spectrum, yields

$$\phi_{uu}(c|k_x) = \frac{1}{\sqrt{2\pi}}\frac{1}{\sqrt{\langle v^2\rangle}}\exp\left[-\frac{1}{2}\frac{(c - U)^2}{\langle v^2\rangle}\right], \tag{3.3}$$

where we note that $\phi_{uu}(k_x, c) = k_x\phi_{uu}(k_x, \omega)$ in this coordinate change. The resulting conditional wavenumber spectrum takes the form of a normal distribution with mean $\mu = U$ and standard deviation, $\sigma = \langle v^2\rangle^{1/2}$. This normal distribution model fits the measured conditional spectrum well, with an r-squared coefficient of determination near 0.99 across the range of wavenumbers with high SNR. This is consistent with previous qualitative comparisons of the shape of the conditional spectrum calculated from LES (Wilczek *et al.* 2015*b*).

The two parameters of the normal distribution, μ and σ, provide a convenient way of quantifying the variation in the spectrum with k_x that is visible in figure 3. The parameters can be obtained directly by integrating the conditional spectrum p.d.f.s, following the usual definition of central moments described in Narita (2017) and Wu & He (2021*a*), according to

$$\mu = \int_{-\infty}^{\infty} c\phi_{uu}(c|k_x, k_z)\,\mathrm{d}c, \quad \sigma^2 = \int_{-\infty}^{\infty}(c - \mu)^2\phi_{uu}(c|k_x, k_z)\,\mathrm{d}c. \tag{3.4a,b}$$

However, for PIV measurements with a prominent noise floor, we found that fitting the conditional spectrum to a normal distribution provided smoother trends with respect to the wavenumber than direct integration (although both methods yield consistent k_x variation). Therefore, the conditional spectrum, $\phi_{uu}(c|k_x)$, at each wavenumber, k_x, was fitted to

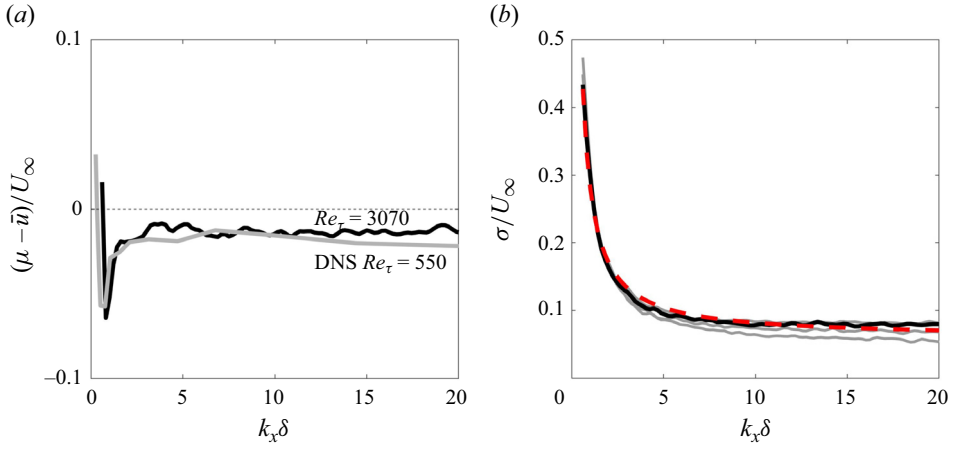

Figure 4. The wavenumber variation of the (*a*) mean, μ, and (*b*) standard deviation, σ, of the conditional spectrum normal distribution, $\phi_{uu}(c|k_x)$ at $y/\delta = 0.2$ in black solid lines. The grey line in (*a*) represents the mean convection velocity c_{u_1} from the DNS of Del Álamo & Jiménez (2009). The grey lines in (*b*) represent other wall-normal locations, to show the very weak dependence on y. The red dashed line corresponds to the analytical model presented in (3.20) with fitted parameters $\langle|\hat{v}(k_v)|^2\rangle^{1/2}/u_\tau \approx 1.3$ and $k_v\delta \approx 3.8$.

a normal distribution with respect to the variable c by a nonlinear least squares routine (using the Levenberg–Marquardt algorithm implemented in Matlab). The resulting μ and σ parameters for each k_x are shown in figure 4(*a*,*b*).

The discrepancy between the mean phase speed, μ, and the local mean velocity, $\bar{u}$, is shown in figure 4(*a*) along with DNS calculations at a lower Re_τ previously reported in Del Álamo & Jiménez (2009). Both show similar trends with most scales convecting slightly slower than the mean velocity at $y/\delta = 0.2$. However, as noted above, the problem of describing and explaining this mean convection velocity has already received significant attention and is provided here primarily for validation purposes.

The width of the phase-speed distribution, σ, as a function of wavenumber has received less focus in past studies and is shown in figure 4(*b*). For high wavenumbers, the distribution width appears roughly constant, consistent with the 1-D version of the random-sweeping model, which assumes that the standard deviation should be some constant associated with the magnitude of the fluctuations of the large-scale advective motions, $\langle v^2\rangle^{1/2}$, which is independent of wavenumber (although can depend on wall-normal location). The independence from wavenumber is a result of the scale-separation assumption of the sweeping model that requires the advecting and advected scales to be sufficiently separated as to be independent, and also a result of the neglect of spanwise wavenumbers in the 1-D formulation.

However, for small wavenumbers, the standard deviation clearly varies quite strongly with k_x. For these LSMs, as k_x increases, the width of the conditional spectrum decreases as k_x^{-1}, indicating that there is more variability in the convection velocity for increasingly larger-scale coherent motions. Wilczek *et al.* (2014) already noted that the 1-D sweeping model predicts constant variance (in the phase-speed domain) in the limit of small wavenumbers, and thus suggested that two possible effects may explain the discrepancy: the absence of scale interactions at large scales and the absence of spanwise wavenumber contribution. Wilczek *et al.* (2015*a*) addressed the spanwise wavenumber assumption and

derived a new expression for the standard deviation that accounts for k_z dependence:

$$\sigma = \left\langle v_x^2 \right\rangle^{1/2} \left[1 + C^2 \left(\frac{k_z}{k_x} \right)^2 \right]^{1/2}. \tag{3.5}$$

Here the ratio of Reynolds stresses is denoted as $C^2 = \langle v_z^2 \rangle / \langle v_x^2 \rangle$ for any fixed wall-normal location. This expression shows the same inverse dependence on k_x visible in the measurements in figure 4(*b*), although it is coupled with a direct dependence on spanwise wavenumber, k_z. Therefore, the three-dimensional (3-D) sweeping model implies that the variance in the convection velocity increases with decreasing k_x but also decreases with decreasing k_z. But this cannot be verified from the streamwise/wall-normal measurements utilized so far. In order to validate this model, and to determine whether there is still a need to consider the role of scale interactions in addition to 3-D effects, we needed to quantitatively compare (3.5) to 3-D spectral measurements from the wall-parallel experiment.

3.3. *Unexplained convection velocity variance from the* (k_x, k_z, ω) *spectrum*

Wall-parallel velocity measurements were used to construct the 3-D spectrum, $\phi_{uu}(\omega, k_x, k_z)$, at a single wall-normal location, $y/\delta = 0.13$. The conditional spectrum, $\phi_{uu}(c|k_x, k_z)$, was then calculated and the standard deviation of the convection velocity was determined as a function of both wavenumbers, $\sigma(k_x, k_z)$, shown in figure 5(*a*). As in figure 4(*b*), we see a strong trend in σ with streamwise wavenumber, k_x, decreasing as the scales become smaller. But now we also observe a relatively weak variation of σ with the spanwise wavenumber, k_z. This weak variation in k_z means it is unlikely that the 3-D sweeping model fully explains the variance trend at lower k_x, since it unavoidably couples the two wavenumbers together as k_z/k_x.

To compare the model in (3.5), we fitted the two model parameters $(\langle v_x^2 \rangle^{1/2}, C) \approx (0.10, 0.56)$ by least squares over the full range of wavenumbers resolved in this experiment to obtain the predicted map of σ shown in figure 5(*b*). The result of the coupling between the two wavenumbers is now quite clear: it is impossible to capture the true k_x variation without also generating an exaggerated k_z variation. The relative errors resulting from the model fit approach 50 % for the lowest wavenumbers in both directions.

The question is how to model the k_x dependence of σ without coupling it to a k_z dependence? The other unexplored source of potential variance is scale interactions. Therefore, we return to the 1-D sweeping model in order to focus on just the streamwise dependence, but now introduce scale interactions in order to generate a k_x dependence that is decoupled from k_z.

3.4. *Wavenumber-dependent sweeping model*

In this section we develop a modification to the 1-D random-sweeping model of Wilczek & Narita (2012) that can capture the k_x dependence of the conditional spectrum width shown in figures 4(*b*) and 5(*a*). We apply the basic procedure of Wilczek & Narita (2012) but now we assume that the advective velocity signal, v, can vary spatially, $v(x)$, such that it possess a Fourier transform in wavenumber space. This spatially varying v extension was first proposed in Kraichnan (1964), although its specific implications on the spectral width were not elaborated. In doing so, we allow for the wavenumbers associated with v to overlap those associated with the turbulence contained in u. Therefore, the v and u

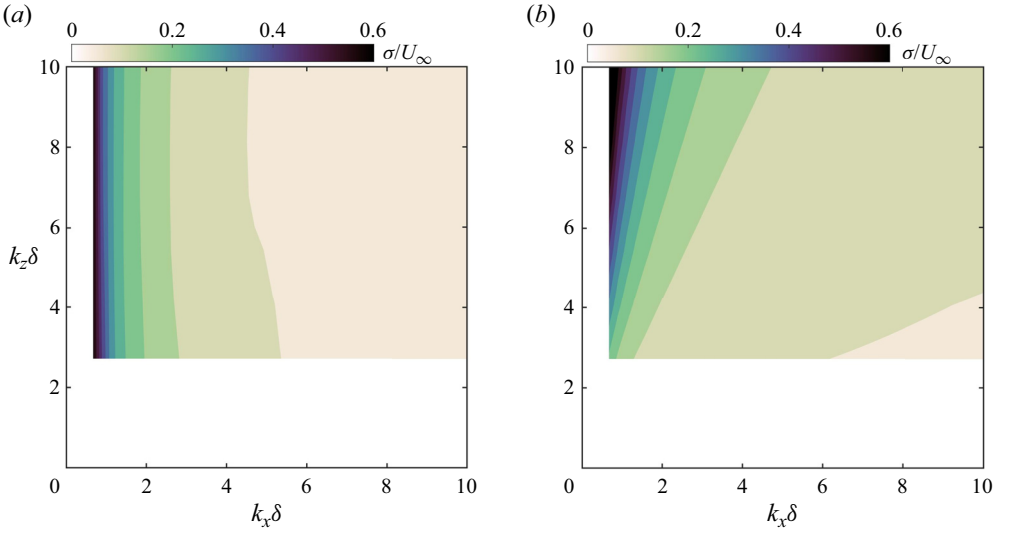

Figure 5. (*a*) Standard deviation of phase speed, $\sigma(k_x, k_z)$, for all streamwise and spanwise wavenumbers calculated from the wall-parallel experiments, showing weak k_z dependence. (*b*) The standard deviation calculated from (3.5), where the fitting constants were obtained from the same wall-parallel experimental data shown in (*a*). In this model, the k_z dependence cannot be separated from k_x.

no longer strictly represent large- and small-scale motions, but rather signals of actively advecting and passively advected structures.

The pure convection equation (3.1) is Fourier transformed from x into spectral space with wavenumber k_x, where the Fourier transform of the velocity $u(x, t)$ is denoted $\hat{u}(k_x, t)$ and the transform of $v(x)$ as $\hat{v}(k_x)$. The resulting momentum equation is then

$$\frac{\partial \hat{u}}{\partial t} + \mathrm{i}k_x U\hat{u} + \sum_{k'} \mathrm{i}(k_x - k')\hat{u}(k_x - k')\hat{v}(k') = 0, \tag{3.6}$$

where the final term is the discrete convolution that results from application of the convolution theorem to the v and u signals. The convolution indicates that only triads of wavenumbers, $(k_x, k', k_x - k')$, participate in the nonlinear interactions. In his earlier proposal of a spatially varying advection signal, Kraichnan (1964) assumed that the fluctuations were confined to a narrow range of large wavenumbers. This assumption appears even more reasonable, now, in light of studies on scale interactions in turbulence that have established that a narrow range of wavenumbers associated just with very-large-scale motions (VLSMs) dominate the observed amplitude modulation effect (see the spectral analysis in Jacobi & McKeon 2013). Based on this, we assumed that the set of triads is highly restricted, such that there is only a single wavenumber k' that interacts with each k_x. This is equivalent to assuming that there is only one wavenumber k' of the v signal that predominantly interacts with each wavenumber $k_x - k'$ to result in the observed energy at wavenumber k_x of the u signal. All the other interactions that could potentially contribute to the energy at k_x are assumed negligible. Because this wavenumber is associated with the v signal, we call it k_v.

In reality, a small but finite set of components of v are involved in scale interactions, and thus we include an $O(1)$ energy scaling factor, C_v, to represent the actual spectral energy associated with the v interactions that are not included in the mathematically simpler,

single wavenumber formulation. Then we write the spectral convection equation as

$$\frac{\partial \hat{u}(k_x)}{\partial t} + \mathrm{i}(k_x - k_v)\hat{u}(k_x - k_v)C_v\hat{v}(k_v) + Uik_x\hat{u}(k_x) = 0. \tag{3.7}$$

In order to solve this initial value problem for $\hat{u}(k_x, t)$, we need to rewrite $\hat{u}(k_x - k_v)$ in terms of $\hat{u}(k_x)$. In the original formulation of the sweeping model, a significant scale separation was assumed between the wavenumbers of the u and v signals, and that was the basis for treating the v signals as spatially uniform with respect to the u. Here, we do not assume spatial uniformity and we allow for k_x and k_v to be close to one another. Therefore, we expand $\hat{u}(k_x - k_v)$ in a Taylor series about k_x in the form $\hat{u}(k_x - k_v) = \hat{u}(k_x) - (\partial\hat{u}(k_x)/\partial k_x)k_v$ and substituting this expansion yields a linear, first-order partial differential equation:

$$\frac{\partial \hat{u}(k_x)}{\partial t} - \mathrm{i}(k_x - k_v)C_v\hat{v}(k_v)\frac{\partial \hat{u}(k_x)}{\partial k_x}k_v + \mathrm{i}(k_x - k_v)\hat{u}(k_x)C_v\hat{v}(k_v) + Uik_x\hat{u}(k_x) = 0. \tag{3.8}$$

This initial value problem can be solved with the initial spectral velocity signal, $\hat{u}(k_x, 0)$, to obtain

$$\hat{u}(k_x, t) = \hat{u}(k_x, 0)\ \exp\left\{-\mathrm{i}k_v tU + \frac{k_v - k_x}{k_v}\frac{U + C_v\hat{v}}{C_v\hat{v}}\left(\mathrm{e}^{\mathrm{i}k_v tC_v\hat{v}} - 1\right)\right\}. \tag{3.9}$$

This velocity signal will result in non-stationary two-point statistics over long times. In order to obtain stationary statistical quantities, we can expand the inner exponential in Taylor series for early times, t, according to $\exp(\mathrm{i}k_v tC_v\hat{v}) - 1 \approx \mathrm{i}k_v C_v\hat{v}t - \frac{1}{2}k_v^2C_v^2\hat{v}^2t^2 + \cdots$ to obtain

$$\hat{u}(k_x, t) \approx \hat{u}(k_x, 0)\exp\left\{-\mathrm{i}k_v tU + \frac{k_v - k_x}{k_v}\frac{U + C_v\hat{v}}{C_v\hat{v}}\left(\mathrm{i}k_v C_v\hat{v}t - \frac{1}{2}k_v^2C_v^2\hat{v}^2t^2 + \cdots\right)\right\}. \tag{3.10}$$

Assuming that the time is early enough such that $k_v C_v|\hat{v}(k_v)|t \ll 1$, we can truncate this approximation and simplify to obtain

$$\hat{u}(k_x, t) = \hat{u}(k_x, 0)\exp\left\{-\mathrm{i}k_v tU + \mathrm{i}t(k_v - k_x)(U + C_v\hat{v})\right\}. \tag{3.11}$$

This early time assumption is equivalent to assuming that the dominant wavenumber of the interacting scale is very low, i.e. that the scale is very large. Therefore, our analysis applies only within the time scale that characterizes the large-interacting structure. Kraichnan (1964) adopted a similar early time assumption and argued that it enforced minimal shear distortion of the u field by v in space.

Now, we employ the two-point time covariance following the procedure described in Wilczek & Narita (2012, Appendix B), which we will eventually transform in the frequency spectrum. We write the spectral quantities at distinct wavenumbers k_x, k_v and k_x', k_v' and times t and $t + \tau$ and, for simplicity, we abbreviate $\hat{u}(k_x', 0) = \hat{u}'$ and $\hat{v}(k_v') = \hat{v}'$,

to obtain

$$\langle \hat{u}(k_x,t)\hat{u}(k_x',t+\tau)\rangle = \left\langle \left[\hat{u}\exp\left(\left\{-\mathrm{i}k_v tU + \mathrm{i}t(k_v-k_x)(U+C_v\hat{v})\right\}\right)\right]\right. \\ \left.\left[\hat{u}'\exp\left(\left\{-\mathrm{i}k_v'(t+\tau)U + \mathrm{i}(t+\tau)(k_v'-k_x')(U+C_v\hat{v}')\right\}\right)\right]\right\rangle \tag{3.12}$$

$$= \left\langle \hat{u}\hat{u}'\right\rangle \left\langle \exp\left(\left\{-\mathrm{i}k_v tU + \mathrm{i}t(k_v-k_x)(U+C_v\hat{v})\right\}\right)\right. \\ \left.\exp\left(\left\{-\mathrm{i}k_v'(t+\tau)U + \mathrm{i}(t+\tau)(k_v'-k_x')(U+C_v\hat{v}')\right\}\right)\right\rangle, \tag{3.13}$$

where we have assumed that the initial conditions are independent of the fluctuating statistics. Then multiplying both sides by the delta function and rewriting in terms of the initial spectral density, we find that

$$\delta(k_x+k_x')\phi_{uu}(k_x',\tau) = \delta(k_x+k_x')\phi_{uu}(k_x',0) \\ \left\langle \exp\left(\left\{-\mathrm{i}k_v tU + \mathrm{i}t(k_v-k_x)(U+C_v\hat{v}) - \mathrm{i}k_v'(t+\tau)U + \mathrm{i}(t+\tau)(k_v'-k_x')(U+C_v\hat{v}')\right\}\right)\right\rangle. \tag{3.14}$$

We integrate over k_x' to eliminate the delta functions and simplify, noting that k_v is also affected indirectly by the delta function due to the triadic relationship (k_x, k_v, k_x-k_v). We also assume, for simplicity, that the dominant structure in the v signal is symmetric in the streamwise direction, such that $\hat{v}(k_v)=\hat{v}(-k_v)$, to obtain

$$\phi_{uu}(-k_x,\tau) = \phi_{uu}(-k_x,0)\mathrm{e}^{\{\mathrm{i}k_x\tau U\}}\left\langle \exp\left(\left\{-\mathrm{i}\tau(k_v-k_x)C_v\hat{v}\right\}\right)\right\rangle \tag{3.15}$$

and taking account of the k_x symmetry of the power spectrum yields

$$\phi_{uu}(k_x,\tau) = \phi_{uu}(k_x,0)\mathrm{e}^{\{-\mathrm{i}k_x\tau U\}}\left\langle \exp\left(\left\{-\mathrm{i}\tau(k_v+k_x)C_v\hat{v}\right\}\right)\right\rangle. \tag{3.16}$$

To evaluate the ensemble average, we need to make use of the definition of the expectation value for the random variable $-\mathrm{i}\tau(k_v+k_x)C_v\hat{v}(k_v)$. This variable is just a scaled version of the ensemble of Fourier coefficients for $\hat{v}(k_v)$. Following Brillinger (2001, theorem 4.4.1), we can treat the distribution of Fourier coefficients of a random stationary signal, v, as a complex normal distribution with zero mean, with variance denoted $\tau^2(k_v+k_x)^2C_v^2\langle|\hat{v}(k_v)|^2\rangle$. Calculating the ensemble average then yields

$$\phi_{uu}(k_x,y,\tau) = \phi_{uu}(k_x,y)\mathrm{e}^{-\mathrm{i}k_x\tau U}\exp\left(-\frac{1}{2}(k_1+k_{1v})^2\tau^2C_v^2\left\langle|\hat{v}(k_v)|^2\right\rangle\right). \tag{3.17}$$

Finally, we Fourier transform this spectral slice from the time domain, τ, to the frequency domain, ω, to obtain a model for the space–time spectrum:

$$\phi_{uu}(k_x,\omega) = \phi_{uu}(k_x,0)\frac{1}{\sqrt{2\pi}}\frac{1}{\sqrt{(k_x+k_v)^2C_v^2\left\langle|\hat{v}(k_v)|^2\right\rangle}}\exp\left[-\frac{1}{2}\frac{(\omega-k_xU)^2}{(k_x+k_v)^2C_v^2\left\langle|\hat{v}(k_v)|^2\right\rangle}\right]. \tag{3.18}$$

This formulation can be reduced to the form reported above in (3.2) for the case where v has no spatial variation, in which case then $\langle|\hat{v}(k_v)|^2\rangle = \langle v^2\rangle$ by Parseval's theorem, and the k_v dependence drops out. But given the presence of a spatially varying v signal, we see that the variance of the p.d.f. now depends on both k_x and k_v.

If we rewrite the frequency dependence, ω, in terms of phase speed, $c = \omega/k_x$, as above, we obtain

$$\phi_{uu}(c|k_x) = \frac{1}{\sqrt{2\pi}} \frac{1}{\sqrt{\left(1 + \frac{k_v}{k_x}\right)^2 C_v^2 \left\langle |\hat{v}(k_v)|^2 \right\rangle}} \exp\left[-\frac{1}{2} \frac{(c-U)^2}{\left(1 + \frac{k_v}{k_x}\right)^2 C_v^2 \left\langle |\hat{v}(k_v)|^2 \right\rangle} \right], \tag{3.19}$$

from which we see that the bandwidth of the space–time spectrum now takes the wavenumber-dependent form

$$\sigma(k_x\delta) = C_v \left\langle |\hat{v}(k_v\delta)|^2 \right\rangle^{1/2} \left(1 + \frac{k_v\delta}{k_x\delta}\right), \tag{3.20}$$

where we have returned to non-dimensional form for comparison with the experimental results above. We note that this wavenumber-dependent analytical result has the inverse k_x dependence anticipated from figure 4(*b*), but without the coupling to the spanwise wavenumber, k_z.

Like in the case of the 3-D sweeping model of Wilczek *et al.* (2015*a*), this 1-D scale-interaction sweeping model has two parameters that determine the value of the conditional spectrum bandwidth, k_v and $C_v\langle|\hat{v}(k_v)|^2\rangle^{1/2}$. The first of these parameters represents the wavenumber, k_v, of the dominant, large-scale contribution to the advection included in the model. The second parameter represents the spectral energy content in that wavenumber, $\langle|\hat{v}(k_v)|^2\rangle^{1/2}$, together with the scale factor, C_v, used to capture energy from other, large scales with analogous behaviour. Although we would expect that generally $k_v < k_x$, in principle there is nothing in the model that requires the large-scale advection mode to be larger than the modes it is advecting in u. And, in particular, we are interested in describing the variation of σ for small k_x where the k_x dependence is apparent; as k_x becomes large, the model predicts that σ converges to a constant value independent of wavenumber.

Fitting the model in (3.20) to the measured σ in figure 4(*b*) at $y/\delta = 0.2$ by linear least squares optimization yields $C_v\langle|\hat{v}(k_v\delta)|^2\rangle^{1/2}/u_\tau \approx 1.3$ and $k_v\delta \approx 3.8$, illustrated as the red dashed line in the figure. The value of $k_v\delta$ corresponds to a large-scale coherent structure for the turbulent boundary layer, $\lambda_v \approx 1.6\delta$, and thus appears consistent with the physical interpretation of the advection equation in (3.1). But we expect these modelling parameters to vary with wall-normal position as the relevant advective scales and energy content of those scales change with y, although that variation is likely to be very subtle given the weak dependence of σ on y shown in figure 4(*b*). We also expect the wavenumber, k_v, and spectral energy, $C_v\langle|\hat{v}(k_v\delta)|^2\rangle^{1/2}$, parameters to be related in a way consistent with other spectral models of wall-bounded turbulence. Therefore, we examine whether the empirical parameters from the scale-interaction model are consistent with these physical trends.

3.5. *Physical motivation and trends for the model parameters*

The parameter, k_v, represents the characteristic length scale associated with the large eddy that is advecting the eddy of size k_x. In the region from the wall and extending out to the location of the VLSM peak, we would expect this scale to be the VLSM scale itself, which exerts a footprint down to the wall (Hutchins & Marusic 2007). Past the VLSM peak, we

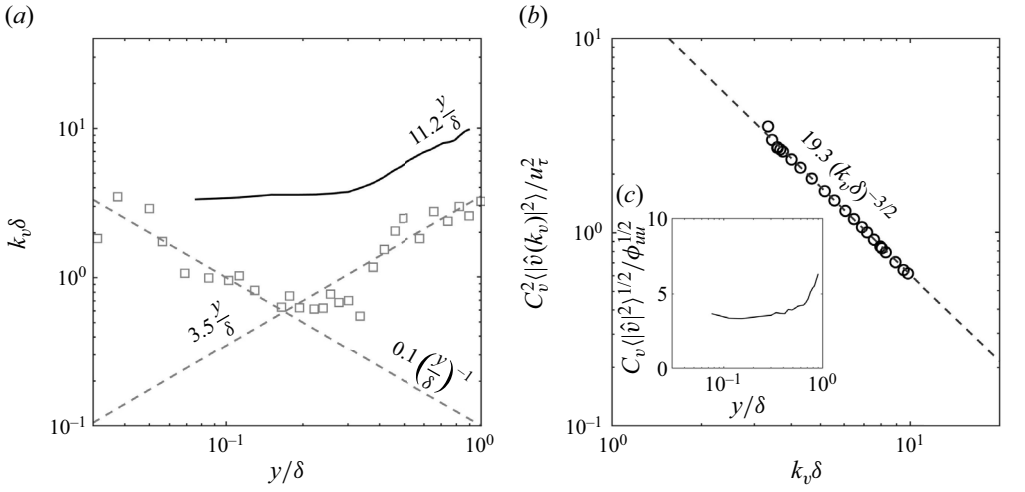

Figure 6. (*a*) The y variation of $k_v\delta$ fitted to the model (3.20) shown by the black line. The grey square points represent the large-scale peak from pipe flow measurements at $Re_\tau = 1649$ in Kim & Adrian (1999); the two dashed lines represent the attached-eddy trend near the wall, and the inverse trend for large scales in the outer region, which is parallel to the model fit. (*b*) The power law between the fitted k_v and the fitted energy spectrum $C_v^2\langle|\hat{v}(k_v)|^2\rangle$ for all wall-normal locations, as a function of k_v. Inset (*c*) shows the estimated value of C_v inferred from the quotient of $C_v^2\langle|\hat{v}(k_v)|^2\rangle$ and $\phi_{uu}(k_x = k_v)$.

expect the energetically dominant large scale to decrease in size linearly with y as reported based on experiments by Kim & Adrian (1999).

Figure 6(*a*) shows the variation of $k_v\delta$ with wall-normal position as the solid black line. Near the wall, the characteristic length scale of the advection according to the model is roughly constant with a value around $k_v\delta \approx 3.8$, consistent with the footprint of a LSM. However, for $y/\delta \gtrsim 0.3$, the wavenumber, k_v, begins to increase linearly with wall-normal height, as Kim & Adrian (1999) observed for the dominant large scale in the outer region of pipe flow experiments. Comparing the trend in $k_v\delta$ with the pipe flow observations (shown in squares), the relevant wavenumber for the model fit tends to be about three times larger than the dominant VLSM scale, $k_v \approx 3k_{VLSM}$, and thus, is better represented by the boundary layer thickness itself in the near-wall region and then by smaller scales farther from the wall. In other words, the empirical k_v represent an intermediate range of energetically dominant wavenumbers between the outer scale and smaller, viscous scales, varying with wall-normal location.

The parameter, $C_v^2\langle|\hat{v}(k_v)|^2\rangle$, represents the spectral energy associated with the dominant large scale of the advection, $\langle|\hat{v}(k_v)|^2\rangle$, and the energy associated with similar, neighbouring scales that is captured through the scaling factor C_v. The expected behaviour of the spectral energy parameter was considered from the perspective of the spectral overlap theory of Perry, Henbest & Chong (1986). For a general, wall-bounded flow, within the log layer, we expect a k_x^{-1} scaling of the spectral energy density as a result of overlap between outer- and attached-eddy length scales, and a $k_x^{-5/3}$ scaling as a result of overlap between attached-eddy and dissipative length scales. Assuming a continuous spectral energy density, we would then expect a spectral scaling k_x^n with exponent, n, between these two limits $-5/3 < n < -1$ for scales that range from outer scales to detached eddies that are larger than dissipative scales. Figure 6(*b*) shows the variation of $C_v^2\langle|\hat{v}(k_v)|^2\rangle$ with $k_v\delta$ and indicates a power law spectral scaling with exponent $-3/2$, consistent with the

range of length scales identified in figure 6(*a*). This power law spectral scaling provides qualitative support for the interpretation of the k_v and $C_v^2\langle|\hat{v}(k_v)|^2\rangle$ parameters in our single wavenumber approximation of the advection signal, v.

The scaling factor C_v is designed to capture the additional energy associated with other interacting large scales of the v signal that was neglected by the single wavenumber mathematical simplification. In order to assess its relative magnitude, independent from the spectral energy associated with the single scale, $\langle|\hat{v}(k_v)|^2\rangle$, we used the streamwise energy spectral density, $\phi_{uu}(k_x, y)$, evaluated at the fitted wavenumbers, k_v, as a means of estimating $\langle|\hat{v}(k_v)|^2\rangle$. Figure 6(*c*) shows $C_v^2\langle|\hat{v}(k_v)|^2\rangle$ divided by $\phi_{uu}(k_x = k_v)$, in order to isolate an approximation of C_v. As expected, C_v is roughly constant across the boundary layer, with a magnitude around 4–6, indicating that the other wavenumbers that contribute to the scale-interaction behaviour similarly (proportionally) to the single dominant wavenumber, k_v.

The spectral trends for the 1-D scale-interaction model shown in figure 6 were also examined for the other Reynolds numbers described in table 1 and the equivalent results are presented in Appendix D. The experiments at all Reynolds numbers demonstrated roughly the same behaviour, but we were not able to identify any trends in the parameter values with respect to the Reynolds number, itself.

Because the 1-D scale-interaction version of the sweeping model does not contain any k_z dependence, the fit displayed in figure 4(*b*) applies for all k_z, consistent with the very weak dependence on k_z shown in figure 5(*a*). In reality, we might expect both the 3-D and scale-interaction effects to contribute, and ideally a combined model could be derived to express both of these effects. But in the present analysis, we are limited to concluding that the scale-interaction model provides an explanation for the increased convection velocity variance at low k_x, without introducing k_z dependence. This appears consistent with experiments, although the exact quantification of the relative contributions of the nonlinear effect remains unknown, and the experiments considered a limited range of spanwise wavenumbers.

Besides examining the variability of the convection velocity, we also investigated the relationship between variations in convection velocity to the average inclination angles of the corresponding velocity modes.

4. Inclination angles, convection velocities and structure size

4.1. *Inclination angles from the space–time cross-spectrum*

The streamwise cross-spectrum between two wall-normal locations has been used by Deshpande *et al.* (2019) to obtain the wavenumber dependence of structure inclination angles, and here we extend their procedure to the 2-D k_x/ω spectrum in order to obtain the simultaneous wavenumber and phase-speed dependence of the inclination angles. Starting from two fluctuating streamwise velocity signals separated in height by Δy, $u(x, t; y)$ and $u(x, t; y + \Delta y)$, we define the cross-spectrum as

$$\phi_{u_y u_{y+\Delta y}}(k_x, \omega; y) = \langle \hat{u}^*(k_x, \omega, y)\hat{u}(k_x; \omega, y + \Delta y)\rangle, \tag{4.1}$$

where $\hat{u}$ denotes the space–time Fourier transform of u, superscript $*$ denotes the complex conjugate and $\langle\cdot\rangle$ denotes the ensemble average over all space–time segments in the ensemble (calculated following the same procedure as the space–time spectrum itself, described in § 3.1). The phase of the ensemble-averaged complex cross-spectrum, θ, is

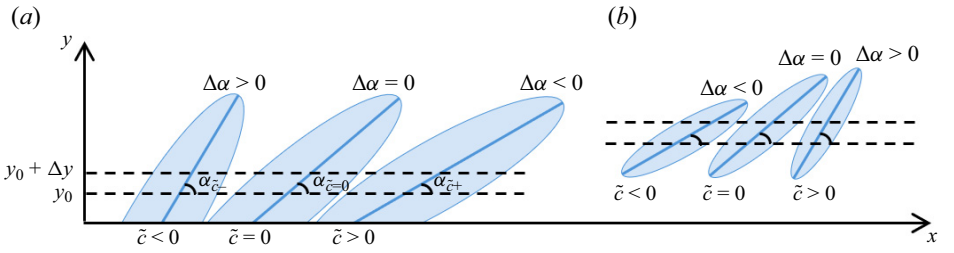

Figure 7. Illustration of the inclination angle, α, calculated from the cross-spectrum between measurements at y_0 and $y_0 + \Delta y$, for modes with three different relative phase speeds, $\tilde{c}$. The relative inclination angle, $\Delta\alpha$, with respect to the inclination angle of the mode with the mean phase velocity, $\tilde{c} = 0$, is also marked. The differing trends for large scales near the wall (*a*) and smaller scales away from the wall (*b*) are explained in § 4.2.

then defined as

$$\theta(k_x, \omega; y) = \tan^{-1}\left\{\frac{\mathrm{Im}\left[\phi_{u_y u_{y+\Delta y}}\right]}{\mathrm{Re}\left[\phi_{u_y u_{y+\Delta y}}\right]}\right\} \tag{4.2}$$

and the average inclination angle, α, measured with respect to the wall, is defined as

$$\alpha(k_x, \omega; y) = \tan^{-1}\left\{\frac{\Delta y}{\Delta x}\right\}, \quad \text{where } \Delta x = -\frac{\theta(k_x, \omega; y)}{k_x}. \tag{4.3}$$

Note that because the cross-spectrum phase is bounded to the branch $-\pi < \theta < \pi$, the measurable inclination angle is also bounded for each wavenumber, k_x, by $\tan^{-1}(k_x \Delta y/\pi) < \alpha < \pi - \tan^{-1}(k_x \Delta y/\pi)$. In other words, the minimum (and maximum) detectable inclination angle magnitudes increase with increasing k_x. Physically, inclination angles smaller than $\pi/2$ indicate downstream inclination, where $\alpha = 0$ aligns with the wall itself; angles greater than $\pi/2$ indicate upstream inclination.

Figure 7 illustrates the geometric sense of the inclination angle defined from the cross-spectrum. Because of resolution limits at high Reynolds number, the near-wall region was not resolved and, thus the origin for the angle measurement, y_0, was fixed to the minimum wall-normal location, $y/\delta \approx 0.04$. The distance between neighbouring points for the inclination calculation was chosen as the spatial resolution in the wall-normal direction, $\Delta y/\delta \approx 0.0375$. But the resulting trends in inclination angle, α, with scale and phase speed were relatively robust to the specific choices of y_0 and Δy. The variation with the choice of y_0 is a result of the changing velocity profile across the boundary layer and will be examined below in figure 9. We also examined doubling the magnitude of Δy and observed no qualitative differences in the inclination angle trends (not shown).

In the analysis below, we employed a normalized phase speed, $\tilde{c} = (c - \mu)/\sigma$, using the average phase speed μ and standard deviation, σ, for each wavenumber k_x. Figure 7 illustrates modes going faster than the mean, $\tilde{c} > 0$, at the mean, $\tilde{c} = 0$, or slower than the mean, $\tilde{c} < 0$. Each of these modes has a corresponding inclination angle, α, and we defined the difference between that inclination angle and the angle associated with modes at the mean phase speed as $\Delta\alpha(k_x, \tilde{c}) = \alpha(k_x, \tilde{c}) - \alpha(k_x, \tilde{c} = 0)$. Then $\Delta\alpha > 0$ indicates a mode that is inclined farther away from the wall than the mode at the mean velocity, and $\Delta\alpha < 0$ indicates a mode inclined shallower with respect to the wall than the mode at the mean velocity.

The interpretation of the inclination angle requires a bit of care due to the potential bias induced by isotropy of small scales. Appendix B discusses the details, but the crucial

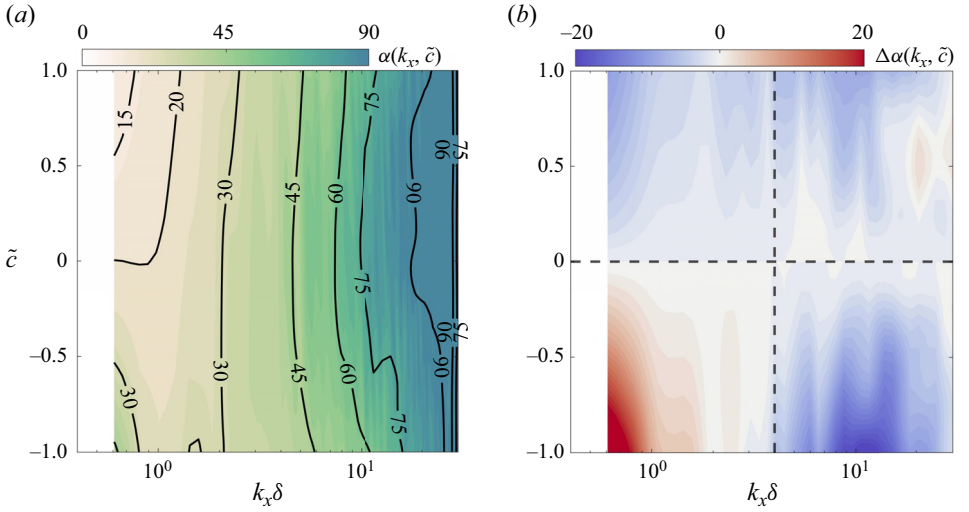

Figure 8. (*a*) Inclination angle α for all wavenumbers and phase speeds within one standard deviation of the mean, $|\tilde{c}| < 1$ at $y/\delta \approx 0.1$. (*b*) The inclination angle deviation from the mean convection velocity, $\Delta\alpha(k_x, \tilde{c}) = \alpha(k_x, \tilde{c}) - \alpha(k_x, \tilde{c} = 0)$, which shows opposite inclination trends for faster and slower moving large-scale structures.

point for the following analysis is that the calculated α represents an upper bound on the inclination angle. This bound is tighter for lower k_x and becomes increasingly loose, biased toward 90° with higher k_x. The confidence in the meaning of α for any given combination of (k_x, c, y) can be determined via appropriate thresholds on the linear coherence spectrum, γ^2, used previously in Deshpande *et al.* (2019) and Baars, Hutchins & Marusic (2017), and only angle measurements with sufficient robustness are included in this analysis.

4.2. *Inclination angle variation with convection velocity*

Applying this cross-spectrum technique, and transforming from ω to $c = \omega/k_x$, we calculated the ensemble average inclination angles for each (k_x, c) pair. Figure 8(*a*) shows the variation in the average inclination angle α with respect to k_x for the range of phase speeds within one standard deviation of the mean, $|\tilde{c}| < 1$. Examining the trend along the mean phase speed, $\tilde{c} = 0$, we note that as the wavenumber increases, there is a steady increase in inclination angle from an angle of approximately 20° for the largest scales up to 90° for the smallest scales. This increase was also observed by Deshpande *et al.* (2019), albeit for just the lower range of wavenumbers. They concluded that the typical attached-eddy inclination angle was 45°, whereas the inclination of large-scale packets was closer to the traditionally assumed 15°. For the small scales, the nearly linear increase in inclination angle with increasing k_x is roughly uniform across all phase speeds, $\tilde{c}$. However, for the LSMs, there is a noticeable variation of inclination angle with phase speed.

Figure 8(*b*) shows the relative inclination angle, $\Delta\alpha$, with respect to that of modes travelling at the mean phase speed. For large scales, $k_x\delta \lesssim 4$, modes moving slower than the mean appear to be more steeply inclined than those convecting at the mean itself, whereas modes moving faster than the mean appear to have shallower inclination to the wall. For small-scale structures, the trend is reversed, albeit weakly.

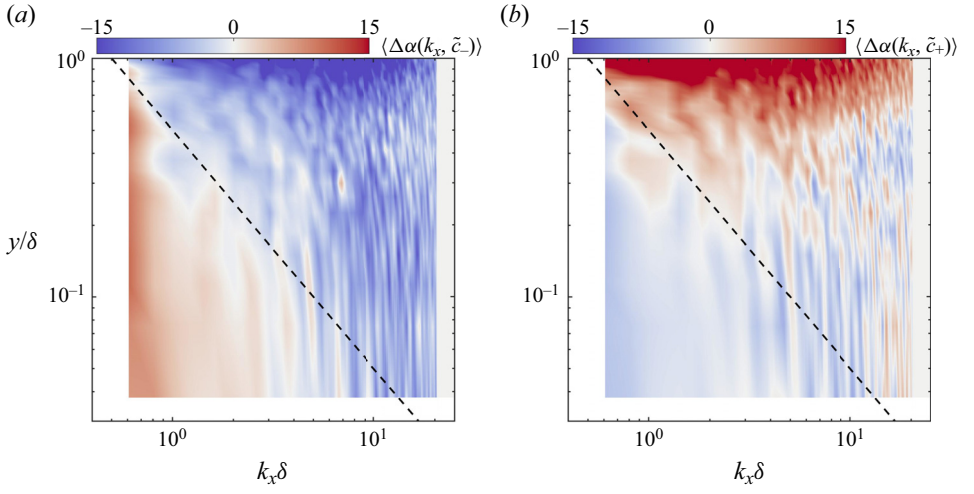

Figure 9. Scale-dependent inclination angle difference, $\Delta\alpha$, averaged over phase speeds (*a*) $\tilde{c} < 0$ and (*b*) $\tilde{c} > 0$, for different wall-normal locations. The black dashed line represents the scale of $k_x\delta = 0.5(y/\delta)^{-1}$ that appears to divide the shear-driven region in the lower-left corner from the eddy-structure region in the upper right.

These trends can be explained in terms of the form of the coherent structures and the mean shear of the flow. Due to their size, the large-scale structures are affected strongly by the mean shear of the boundary layer, which elongates and inclines coherent motions near the wall, as noted by Li *et al.* (2022). As these structures convect faster, the relative effect of the mean shear across the structure height becomes stronger, resulting in increased inclination toward the wall.

By contrast, the small-scale structures are not as strongly distorted by the mean shear. As they convect faster, they experience an associated increase in inclination angle that we speculate is a consequence of the asymmetry of the eddy shape itself. For instance, in Theodorsen's classic hairpin vortex shape, the geometry of the two legs is substantially different from the head. And more generally, depending on the eddy composition (e.g. the orientation of pairs of prograde and retrograde vortices, see Natrajan, Wu & Christensen 2007), different spatial regions of an eddy can experience different accelerations from purely kinematic considerations, resulting in a change of inclination even in the absence of a mean shear. Of course, eddy dynamics may also be an important consideration beyond kinematics, but we focus here on the simplest considerations that can fit the observations.

According to this proposed explanation, the cutoff wavenumber, k_x, between eddies whose inclination is shear dominated versus eddies whose inclination is due to their vortex structure should vary with wall-normal location, y, as the strength of the mean velocity gradient varies. Furthermore, for a logarithmic velocity profile, where the velocity gradient scales as y^{-1}, we would expect the cutoff wavenumber to vary according to $k_x \sim y^{-1}$. To test this hypothesis, we averaged the profile of $\Delta\alpha$ separately over the positive and negative phase-speed deviations, weighted by the spectral energy, $\phi_{uu}(k_x, c)$, to obtain $\langle\Delta\alpha(k_x, \tilde{c}_-)\rangle$ for $\tilde{c} < 0$ and $\langle\Delta\alpha(k_x, \tilde{c}_+)\rangle$ for $\tilde{c} > 0$. These average trends in the inclination angle discrepancy were then plotted against wall-normal location, as shown in figure 9(*a*,*b*).

For the case of slower than average phase speeds, shown in figure 9(*a*), we find clear evidence for a shear-dominated region near the wall, at lower wavenumbers, where the

inclination angle variation, $\Delta\alpha$, is opposite (red) in sign to the phase-speed variation, $\tilde{c}$. This shear region appears to be confined by $k_x \lesssim y^{-1}$. Outside of the region, the sign between $\Delta\alpha$ and $\tilde{c}$ is reversed (blue), where we speculate that the inclination angle change is largely determined by the eddy vortex structure and not the shear. For the case of faster than average phase speeds, shown in figure 9(*b*), the same trends appear, although the evidence for the $k_x \lesssim y^{-1}$ cutoff is weaker. These distinct regions also appear across other Reynolds numbers, as illustrated in Appendix D. This general trend is also shown in figure 7, for large-scale, near-wall structures (right) compared with small-scale, outer structures (left).

To further support the above claim that eddy geometry and mean shear are key factors in explaining the inclination angle/phase-speed trends, we develop a crude kinematical model based on an asymmetric rigid 'eddy' in Appendix E. The model illustrates how the shear-driven inclination effect and the vortex structure inclination effect can result in opposite behaviour with respect to small changes in the convection velocity of an eddy. More detailed examination of the fine structure of instantaneous eddies is still needed to provide additional validation for these observations. But the basic variation of inclination angle across structures with different phase speeds appears to be the result of competing physical mechanisms in the turbulent boundary layer.

5. Conclusions

Understanding the scale-dependent convection velocities of coherent structures in wall-bounded turbulence is crucial for both the fundamental problem of modelling turbulent flows and for the practical task of transforming temporal experimental measurements into meaningful spatial descriptions. Significant research efforts have been devoted towards quantifying scale-dependent mean convection velocities and their deviations from Taylor's frozen turbulence hypothesis, but less attention has been paid toward the statistical variation in convection velocities about their mean. In the last decade, efforts at modelling the space–time turbulence spectrum have suggested that the spectral width in the frequency domain, which corresponds to the variation in phase speeds, can be associated with fluctuations in the large-scale advective motions in the flow. But these models did not consider the scale dependence of the phase-speed variability or the physical consequences of that variability.

In the present study, we first calculated the 2-D space–time spectra of turbulent boundary layers in the range of $Re_\tau = 530$–3070 and validated the measurements against hotwire and DNS calculations, to within the attenuation limits of PIV. We then transformed the frequency domain, ω, into phase speed, c, and calculated the conditional spectra in order to observe the variation in its phase-speed width, σ, with wavenumber, k_x. Using this experimental data, we arrived at the following four primary conclusions.

(i) We noted that the largest-scale motions exhibit the highest variability in phase speeds, and that variability decreased inversely with streamwise wavenumber until it saturated at a constant level for small-scale motions. Wilczek *et al.* (2014) had suggested that the k_x dependence of spectral width could be the result of scale interactions or 3-D effects, and they generated a model for the latter.

(ii) We showed that this 3-D sweeping model couples the spanwise and streamwise wavenumbers together in a stronger way than was observed in our wall-parallel experiments, and thus we considered the possibility that scale interactions in one dimension could better explain the variation in spectral width with k_x alone.

(iii) By extending the 1-D random-sweeping model of the space–time spectrum developed by Wilczek & Narita (2012) to allow for scale interactions between the large sweeping motions and the small-scale turbulence, we obtained a simple analytical description of the k_x-dependent spectral width that depended on two parameters: the wavenumber of the LSMs, k_v, and the corresponding spectral power, $C_v^2\langle|\hat{v}(k_v)|^2\rangle$. And importantly, this model for the variance was not coupled to the spanwise wavenumber. We then showed that the empirical values of these two parameters were consistent with their physical interpretations within the proposed model. The wavenumber, k_v, identified a range of energetically dominant large-scale modes, and the spectral power, $C_v^2\langle|\hat{v}(k_v)|^2\rangle$, was related to the wavenumber via a power law scaling that was consistent with spectral similarity theory.

Despite the consistency of the 1-D scale-interaction sweeping model and its ability to describe the phase-speed variance for large scales without a coupled k_z dependence, it was impossible to quantitatively separate the 3-D and scale-interaction effects on the phase-speed variance, which may both contribute to the true convection velocity variance.

After modelling the k_x dependence in the phase-speed variance, we then explored the physical consequences of a distribution of different phase speeds for a given wavenumber. Using the cross-spectrum between space–time measurements at two adjacent wall-normal locations in the boundary layer, the structure inclination angles were calculated as a function of wavenumber and phase speed. Consistent with previous observations by Deshpande *et al.* (2019), we found an increasing inclination angle with decreasing scale size.

(iv) We also noted variation in inclination angles with phase speed for the large-scale structures. Velocity modes moving slower than the mean phase speed for their size tended to be inclined away from the wall more than faster moving modes. The variation in inclination angle was described as a consequence of shear-driven stretching of large eddies in proportion to their convective velocity, and this explanation appeared to capture important qualitative features of the observed phase-speed variation.

The research provides both a simple model to describe the scale-dependent variability in phase speeds of coherent motions, as well as a heuristic picture of how variations in phase speed are associated with variations in modal inclination angles via a shearing mechanism. These results may allow for improving turbulence models that depend on the superposition of velocity modes with varying phase speeds, and for understanding how the choice of phase speeds is be expected to impact velocity mode geometries.

Acknowledgements. The authors thank the anonymous referees for important suggestions about the difference between variance models based on 3-D effects versus scale interactions, as well as comments about the spectral relationship between the two model parameters.

Funding. The authors gratefully acknowledge the support of Israel Science Foundation grant 219/21.

Declaration of interests. The authors report no conflict of interest.

Author ORCIDs.
G. Cui https://orcid.org/0000-0003-2159-2765;
I. Jacobi https://orcid.org/0000-0001-7377-8292.

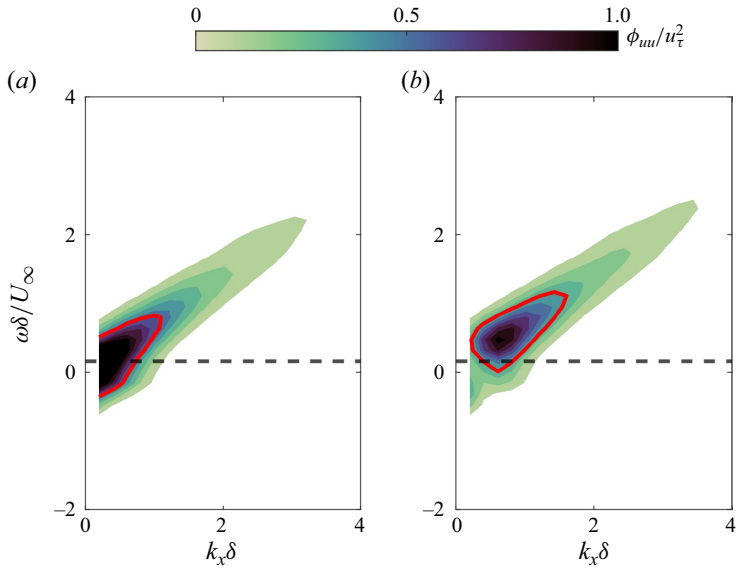

Figure 10. The 2-D spectral energy density for $Re_\tau = 3070$ at $y/\delta \approx 0.1$ with mean subtraction of (*a*) the global ensemble mean; and (*b*) the local mean of each sample within the ensemble. Due to symmetries of the 2-D spectral density, the integral over any half-plane includes half of the total streamwise velocity variance, $\overline{u'^2}$, at the corresponding height, and the spectra have been normalized accordingly. The red line represents the isocontour of spectral energy density containing 30 % of the total streamwise energy.

Appendix A. Mean subtraction in spectral calculations

There are two approaches to mean subtraction when calculating the turbulence spectra that yield different results, particularly with respect to the large-scale energy. LeHew *et al.* (2011) calculated the 2-D spectral density of the streamwise velocity fluctuations from ensemble PIV measurements where the global mean velocity across the entire ensemble was removed, following the standard procedure recommended in Bendat & Piersol (2010). This procedure applied to the current measurements shown in figure 10(*a*). However, because the velocity signals are not strictly stationary (the mean varies slightly across the different samples of the ensemble), subtraction of the global mean results in spectral energy at zero frequency/wavenumber (as noted in LeHew 2012).

This energy in the zero frequency component represents the average squared deviation of the sample means, $\bar{u}_n$, from the global ensemble mean, $\bar{u}$, given by $\langle(\bar{u}_n - \bar{u})^2\rangle$, and is a measure of the non-stationarity of the record (Otnes 1978). Unfortunately, this DC component of the spectrum leaks into neighbouring low frequencies/wavenumbers resulting in the appearance of spurious energy density at a range of large scales, including scales larger than the measurement domain itself, which obviously were not experimentally resolved. More problematically, in the case of LeHew *et al.* (2011), this spurious energy appears for negative frequencies, indicating (perhaps misleadingly) that a non-negligible amount of the spectral energy is associated with upstream-travelling structures.

Because of the problem of DC spectral leakage, an alternative approach to spectral estimation involves subtracting the local mean of each sample prior to the Fourier transform, instead of removing the global ensemble mean. Local mean subtraction has been widely employed (Nikias & Raghuveer 1987; Keisler 1976) and has been

recommended as the preferable approach by Saunders & Hamrick (1982). Figure 10(*b*) shows the current measurements processed accordingly.

By subtracting the local mean, zero spectral energy is explicitly enforced at zero frequency/wavenumber, and thus no spurious energy appears at neighbouring large scales, and the 2-D spectral density appears shifted away from the origin (in both directions) with the maximum energy density centred near the size of the measurement domain itself. Importantly, we note that without the DC spectral leakage, the energy density associated with upstream-travelling structures (negative frequencies) is indeed negligible, as would be expected for large-scale coherent structures travelling downstream.

In this study we have adopted the local sample mean subtraction in order to avoid the spurious large-scale energy leakage, albeit at the cost of obscuring the deviations from stationarity within the ensemble. The energy excluded by this choice can be quantified by comparing the energy of the non-stationarity to the energy of fluctuations assuming stationarity, as

$$\frac{\langle(\bar{u}_n - \bar{u})^2\rangle}{\overline{u'^2}} \approx 9\,\%, \tag{A1}$$

and this compares well with the 12 % of total TKE that was attributed to upstream-travelling waves in LeHew (2012) due to their use of the global mean.

Appendix B. The interpretation of the inclination angle from the cross-spectrum

In figure 8(*a*) the trend of increasing inclination angle with wavenumber was noted, and caution was called for regarding its interpretation. Figure 11(*a*) shows that trend more clearly for just the mean phase speed, $\tilde{c} = 0$. As noted in the main text, the interpretation of this inclination angle trend requires some care because α is the result of an ensemble-averaged spectra that reflects changes in the dominant inclination angle of structures but also increased variability of the inclination angle across the ensemble and increased isotropy of the structures, both of which can bias the average inclination angle.

Deshpande *et al.* (2019) used the spectral coherence, γ^2, utilized in Baars *et al.* (2017), as a method to threshold the significance of measurements inferred from the cross-spectrum. The spectral coherence can be written as

$$\gamma\,(y; k_x, \omega) = \left| \underbrace{\left\langle \left(\frac{|\hat{u}\,(y; k_x, \omega)\,|\,|\hat{u}\,(y + \Delta y; k_x, \omega)\,|}{\left\langle |\hat{u}\,(y; k_x, \omega)|^2 \right\rangle^{1/2} \left\langle |\hat{u}\,(y + \Delta y; k_x, \omega)|^2 \right\rangle^{1/2}} \right) \mathrm{e}^{\mathrm{i}\theta} \right\rangle}_{\textit{amplitude weighting}} \right|, \tag{B1}$$

where the ensemble average is performed over the product of the complex phase angle between the two measurements, in the form $\mathrm{e}^{\mathrm{i}\theta}$, and a weighting function that describes the amplitude of the spectral signals at the two measurements. Without the weighting factor, the coherence is just the mean resultant length of the phase angle vectors, R, from circular statistics (Fisher 1995) defined as

$$R = \left| \left\langle \mathrm{e}^{\mathrm{i}\theta} \right\rangle \right|, \tag{B2}$$

which is related directly to the variance of the phase angle, $V_\theta = 1 - R$. Therefore, $(1 - \gamma)$ is a weighted measure of the variance of the cross-spectrum phase (since γ is bounded between [0, 1]).

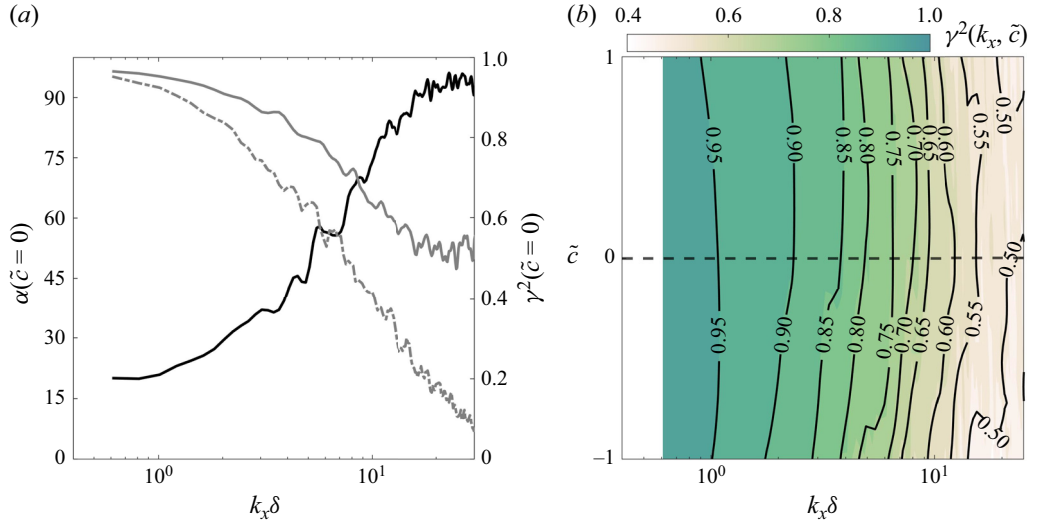

Figure 11. (*a*) Inclination angle α calculated from the cross-spectrum defined in (4.3) (black solid line) and coherence, γ^2 (grey solid line) at $\tilde{c} = 0$ and $y/\delta \approx 0.1$. A synthetic coherence calculated with the same amplitude but uniform randomly distributed phase angles is shown in the dashed line. (*b*) The full coherence map for the phase-speed range, $|\tilde{c}| \leq 1$, at the same wall-normal location corresponding to the inclination angle map shown in figure 8(*a*).

If we assume that the phase difference θ is uniform for all signals in the ensemble, then we can consider the effect of just the amplitude weighting contribution. The weighting depends on the extent of a k_x-sized structure in the y direction: if the structure is highly anisotropic and, thus extends far along its axis of inclination, the amplitude weighting will be unaffected as the spectral amplitude at both locations can be comparable. But as the structure becomes more isotropic and, thus extends less far along its axis of inclination (i.e. takes on a more spherical shape), this will necessarily suppress the amplitude weighting that is based on two measurements separated by Δy, since the spectral amplitude at one location will necessarily be substantially different than the amplitude at its neighbour. So, for a fixed inclination angle, we would expect γ to decrease with increasing k_x as smaller scales become more isotropic, until γ hits an isotropic floor. This floor could also be influenced by the noise floor from the PIV measurements that is assumed isotropic at high wavenumbers. The grey line in figure 11 shows the coherence versus wavenumber (on the right axis) and the isotropic floor of γ^2 is clearly visible for wavenumbers $k_x\delta \gtrsim 20$.

On the other hand, if we assume that the weighting is fixed and uniform, but the θ is randomly distributed, then $\gamma = 0$. In other words, in order for γ to decrease below the isotropy floor, there must be a significant variance in the phase angles, θ. The dashed line in figure 11 shows a synthetic coherence, γ^2, calculated by randomizing the phase angles in the ensemble average while keeping the weighting unchanged, and the coherence descends to zero for the high wavenumbers, as expected.

In the region of the isotropy floor of the coherence, we expect to measure an inclination angle of 90°, irrespective of the true inclination of the structures, as a consequence of structure isotropy, as illustrated geometrically in Appendix C, and that is exactly what we find in the black line for α in that wavenumber range. For inclination angle measurements outside of this isotropy region, we expect the inclination angle to be biased upwards

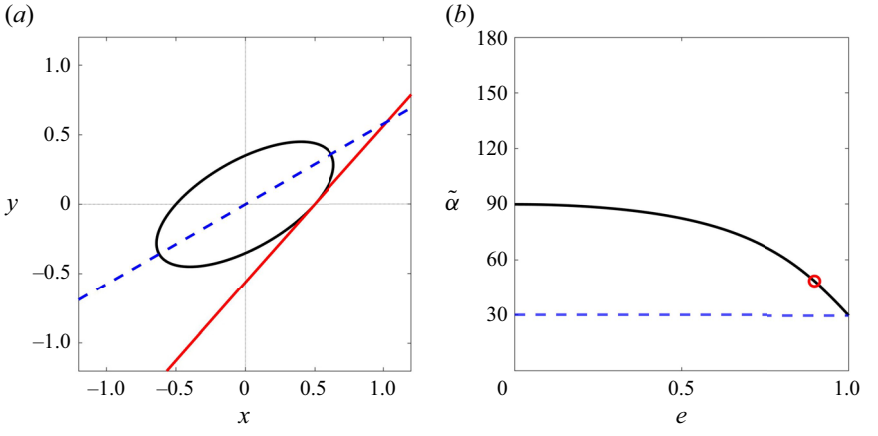

Figure 12. Illustration of how the eccentricity affects the inclination angle measurement. (*a*) An ellipse with true inclination angle of 30° marked by the blue dashed line along its inclination axis, and the measured inclination marked by the solid red line that is tangent to its boundary at the measurement location $y = 0$. The width of the ellipse is fixed as the wavelength of the structure. (*b*) The measured inclination angle, $\tilde{\alpha}$, is shown as a function of the eccentricity of the ellipse, in solid black, compared with the true inclination angle marked with the dashed blue line. For increasing isotropy, the measured inclination tends to 90°.

towards 90° due to the isotropy effect, even when the phase angle is well defined (i.e. even when the coherence is above the synthetic coherence threshold for random phases).

In light of this, we should interpret α as an upper bound on the mean inclination angle, as long as the corresponding coherence γ exceeds both its random-phase value and its isotropy floor. The larger the wall-bounded coherent structure is, the less isotropic, and the closer α is to capturing a realistic inclination angle; the smaller and more isotropic the structure, the closer α approaches an upper bound on the inclination angle.

In the main text we included only inclination angles that satisfied these coherence criteria, keeping in mind the bias that may occur with increasing wavenumber. A map of the coherence values corresponding to the inclination angle map of figure 8(*a*,*b*) is shown in figure 11(*b*) to confirm that the entire range of phase speeds within one standard deviation of the mean, $|\tilde{c}| < 1$, satisfies the coherence threshold requirements. (The values of coherence shown here are substantially higher than those appearing in Deshpande *et al.* (2019) due to the small, fixed value of Δy used here versus the larger, variable wall-normal displacement used in their study.)

Appendix C. Isotropy and inclination angle detection

In order to illustrate the difficulty of detecting inclination angles from highly isotropic structures, we consider a simple geometrical model of a 2-D eddy. Here it is represented by an elliptical region of space with high correlation of some flow variable, i.e. an elliptical coherent structure, with the centre at (x_0, y_0) (taken here without loss of generality to be the origin), major axis a and minor axis b, such that $a \geq b$ and eccentricity $e = \sqrt{1 - (b/a)^2}$, shown in figure 12(*a*). The inclination angle of the ellipse, α, is measured from the positive x axis to the major axis a, in the first quadrant. The wavelength of the structure, λ, is the diameter of the ellipse measured at $y = 0$.

The general equation of a tilted ellipse is given in polar coordinates (r, θ) as

$$r = \frac{ab}{\sqrt{[b\cos(\theta-\alpha)]^2 + [a\sin(\theta-\alpha)]^2}}. \tag{C1}$$

Solving for the major and minor axis, (a, b) in terms of the fixed wavelength and eccentricity, (λ, e), i.e. for the case where $(r, \theta) = (\lambda/2, 0)$, yields

$$a = \frac{\lambda}{2\sqrt{2}}\sqrt{\frac{e^2 - 2 + e^2\cos(2\alpha)}{e^2-1}}, \tag{C2}$$

$$b = \frac{\lambda}{2}\sqrt{1 - e^2\cos^2(\alpha)}. \tag{C3}$$

Finally, to solve for the slope of the ellipse based on its centre of mass, we can calculate $\mathrm{d}y/\mathrm{d}x$ along $y = y_0$, or expanding

$$\frac{\mathrm{d}y}{\mathrm{d}x} = \frac{\partial y}{\partial r}\left(\frac{\mathrm{d}x}{\mathrm{d}r}\right)^{-1} + \frac{\partial y}{\partial \theta}\left(\frac{\mathrm{d}x}{\mathrm{d}\theta}\right)^{-1}, \tag{C4}$$

where $x = r\cos(\theta)$ and $y = r\sin(\theta)$. Solving and substituting for $\theta = 0$ yields

$$\left.\frac{\mathrm{d}y}{\mathrm{d}x}\right|_{(\lambda/2,0)} = \frac{b^2\cot(\alpha) + a^2\tan(\alpha)}{a^2 - b^2} \tag{C5}$$

$$= \frac{(1-e^2)\cot(\alpha) + \tan(\alpha)}{e^2} \tag{C6}$$

and, therefore, the inferred/measured inclination angle, $\tilde{\alpha}$, is given by

$$\tilde{\alpha}(\alpha, e) = \tan^{-1}\left(\frac{(1-e^2)\cot(\alpha) + \tan(\alpha)}{e^2}\right), \tag{C7}$$

and we can see that in the limit as $e \to 1$ (very elongated structures), $\tilde{\alpha} \to \alpha$ and in the limit as $e \to 0$ (symmetric, isotropic structures), then $\tilde{\alpha} \to \pi/2$, as shown in figure 12(*b*). Thus, we expect to obtain 90° inclination angles for structures with low anisotropy, consistent with the discussion of the small-scale coherence in Appendix B.

Appendix D. Reynolds number variation

The observations about the variation in phase speed and the relationships between phase-speed variability and inclination angle were studied at all of the Reynolds numbers described in table 1, although the main text includes only the results for the highest Reynolds number.

Figure 13 is the companion for figure 6 that illustrates the trends in the two fitting parameters, k_v and $C_v^2\langle|\hat{v}(k_v)|^2\rangle$, with wall-normal location. In the main text, these two trends were explained in terms of the dominant large-scale wavenumbers and the spectral similarity theory between wavenumbers and the energy distribution, respectively. We observe similar results across all of the Reynolds numbers, although no distinct trends with Reynolds number were obtained due to the limited range of flow velocities considered.

Figure 14 is the companion for figure 9 that illustrates the relationship between the inclination angle variation and phase-speed variation for phase speeds slower than

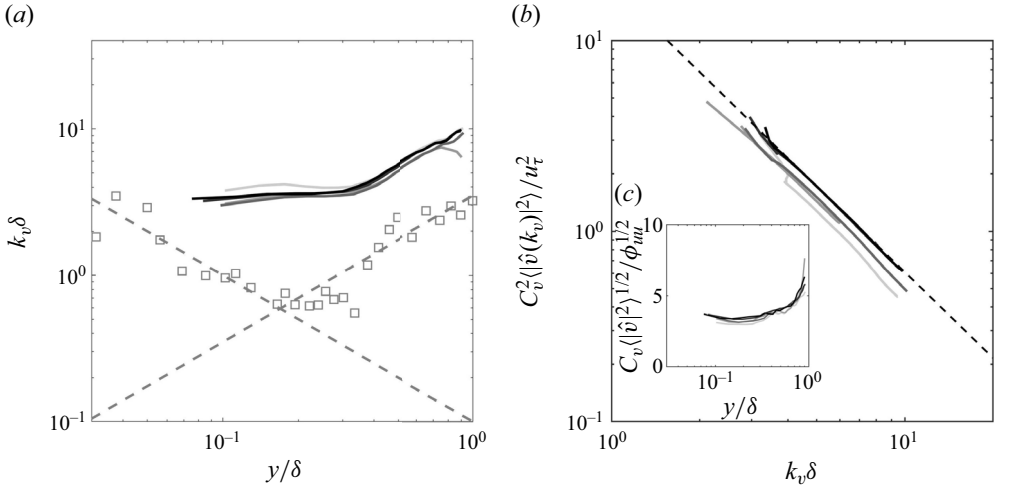

Figure 13. The same results as shown in figure 6 but for all five Reynolds numbers; darker shades of grey correspond to increasing Re_τ. The wavenumber and wall-normal trends are robust across experiments at different Reynolds numbers.

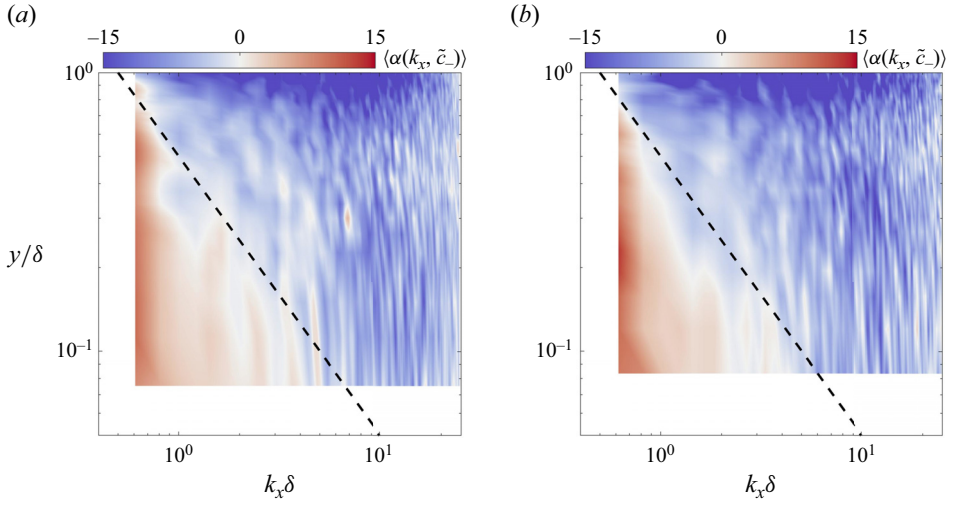

Figure 14. Scale-dependent inclination angle difference, $\Delta\alpha$, averaged over phase speeds for $\tilde{c} < 0$ for (*a*) $Re_\tau = 3070$ and (*b*) $Re_\tau = 2410$, for different wall-normal locations. The black dashed line represents the scale of $k_x\delta = 0.5(y/\delta)^{-1}$ that appears to divide the shear-driven region in the lower-left corner from the eddy-structure region in the upper right.

the average, $\tilde{c} < 0$, for Reynolds number $Re_\tau = 3070$ (figure 14*a*) and $Re_\tau = 2410$ (figure 14*b*). As the Reynolds number decreases, the shear-driven region moves to slightly lower wavenumbers, consistent with the u_τ dependence predicted in the rigid 'eddy' model in Appendix E. The other Reynolds number cases showed the same behaviour and are not reproduced here.

Appendix E. Inclination angle model with rigid 'eddy' kinematics

In order to obtain a very crude picture of the relationship between variations in inclination angle and convection velocity, we model a coherent eddy as a rigid body moving with velocity c in a turbulent flow with convection velocity U, with characteristic length scale $\lambda_x = 2\pi/k_x$ and moment of inertia I. Like studies of vortex rings (Gan, Dawson & Nickels 2012), we further assume that the rigid eddy has independent, signed drag coefficients, C_i, at its head, C_h, and feet, C_f, defined by

$$C_i = \frac{F_i}{\frac{1}{2}\rho\lambda_x^2(U_i - c)^2}, \tag{E1}$$

where U_i is the local mean velocity near the head or feet. The mean velocity can be expanded in Taylor series about the centre of mass of the body as $U_i = U_0 \pm U_y(\lambda/2)$ for the head $(+)$ and the feet $(-)$, where U_y is the velocity gradient in the y direction evaluated at the centre of mass. The force is taken as positive in the streamwise direction when $(U_i - c) > 0$, as reflected in the drag coefficient sign. For a representative case of a structure whose head is accelerated by the surrounding upper flow and feet are decelerated by the surrounding lower flow, $C_h > 0$ and $C_f < 0$.

Treating the centre of mass as a fulcrum, the torques at the head and feet are defined as

$$\tau_h = -\frac{\lambda_x}{2}F_h, \quad \tau_f = \frac{\lambda_x}{2}F_f, \tag{E2a,b}$$

and then the angular acceleration about the fulcrum, a, can be written as

$$a = I^{-1}\left(\tau_h + \tau_f\right), \tag{E3}$$

such that when the head experiences a greater positive force than the feet, the body accelerates in the negative angular direction, $a < 0$, i.e. the body would tend to roll forward. Therefore, this net torque would tend to incline the body further towards the wall, and thus, a negative acceleration, $a < 0$, corresponds to a reduction in the inclination angle, $\Delta\alpha < 0$.

Substituting the force definitions into the angular momentum balance in (E3), we obtain

$$a = -\frac{I^{-1}\rho\lambda_x^2}{2}\left[C_h\left(U_0 + U_y\frac{\lambda_x}{2} - c\right)^2 - C_f\left(U_0 - U_y\frac{\lambda_x}{2} - c\right)^2\right]. \tag{E4}$$

Then we perturb the angular acceleration and convection velocities (a, c) to $(a + \Delta a, c + \Delta c)$, linearize and subtract the unperturbed angular momentum balance, to obtain

$$\Delta a = \frac{I^{-1}\rho\lambda_x^2}{2}\left[(C_f + C_h)\lambda_x\frac{\mathrm{d}U}{\mathrm{d}y} + 2(C_f - C_h)(c - U_0)\right]\Delta c. \tag{E5}$$

Assuming the typical case noted above for $C_h > 0$ and $C_f < 0$, we note that $(C_f - C_h) < 0$. We further assume asymmetry between the head and feet, such that the feet have a larger magnitude drag coefficient than the head due to their shape or orientation, and then $(C_f + C_h) < 0$ also. Writing these two quantities explicitly with their typical signs, we can simplify

$$\Delta a = \left(\frac{I^{-1}\rho\lambda_x^2}{2}|C_f + C_h|\right)\left[-\lambda_x\frac{\mathrm{d}U}{\mathrm{d}y} + 2\frac{|C_f - C_h|}{|C_f + C_h|}(U_0 - c)\right]\Delta c, \tag{E6}$$

where the quantity in parenthesis is always positive and the sign of the term in brackets depends on the balance between its two contributions.

The first term in the brackets, $-\lambda_x(\mathrm{d}U/\mathrm{d}y)$, represents acceleration of the body due to the mean shear, which is relevant when the shear is sufficiently strong and the body is large enough to be affected by the shear directly. If this term alone dominated the acceleration then we would expect $\Delta a \sim -\Delta c$ in the region of large structures and high shear, i.e. we would expect structures moving faster than typical to be inclined closer to the wall.

The second term in the brackets, $2(|C_f - C_h|/|C_f + C_h|)(U_0 - c)$, applies even in the absence of any mean shear or for scales that are so small that the mean shear does not affect them directly. This term represents variation in the acceleration of the structure due to the asymmetry of its shape, i.e. differences in the drag coefficient between the head and feet of the eddy. For instance, this might be the result difference between the drag coefficients of prograde and retrograde vortices that constitute a coherent structure (Natrajan *et al.* 2007). For most of the logarithmic region of the boundary layer, $(U_0 - c) > 0$; evidence of this can be seen from the plot of the mean convective velocity, μ at $y/\delta = 0.2$ in figure 4(*a*). Therefore, if this term were dominant, then we would expect $\Delta a \sim +\Delta c$, such that structures moving faster than typical become more inclined upward from the wall. In the limit of perfect asymmetry, $C_f = -C_h$, the vortex shape term becomes unbounded in this simplified model.

In general, both of these effects – shear and vortex structure – could be relevant, in which case it is the balance between them that determines the sign of the relationship between Δa and Δc. When the shear effect is sufficiently strong, $\Delta a \sim -\Delta c$, and that occurs when

$$-\lambda_x \frac{\mathrm{d}U}{\mathrm{d}y} + 2\frac{|C_f - C_h|}{|C_f + C_h|}(U_0 - c) < 0, \tag{E7}$$

$$\lambda_x \frac{\mathrm{d}U}{\mathrm{d}y} > 2\frac{|C_f - C_h|}{|C_f + C_h|}(U_0 - c). \tag{E8}$$

This result can be made more specific by assuming a logarithmic velocity profile with friction velocity u_τ and Kármán constant κ to obtain

$$k_x < \left(\frac{\pi}{\kappa}\frac{u_\tau}{(U_0 - c)}\frac{|C_f + C_h|}{|C_f - C_h|}\right)\frac{1}{y} \quad \text{for } \Delta a \sim -\Delta c. \tag{E9}$$

This criterion on $k_x y$ establishes a region where the eddy is inclined predominantly by the effect of the velocity gradient due to its large size. Outside of this region, for smaller structures or in low-shear regions far from the wall, the opposite relationship is obtained, $\Delta a \sim \Delta c$, which is likely a consequence of the detailed structure of the eddies, here represented naively by the two drag coefficients. The separating line between the shear and eddy-structure regions is $k_x \sim y^{-1}$, as illustrated by the dashed lines in the maps shown in figures 9 and 14.

It is worth reiterating that this model is based on crude kinematic considerations of a rigid eddy, and is designed only to provide the intuition that the effect of shear and the effect of eddy-structure/vortex geometry can produce opposing inclination trends.

References

Baars, W.J., Hutchins, N. & Marusic, I. 2017 Self-similarity of wall-attached turbulence in boundary layers. *J. Fluid Mech.* **823**, R2.

Banerjee, T. & Katul, G.G. 2013 Logarithmic scaling in the longitudinal velocity variance explained by a spectral budget. *Phys. Fluids* **25** (12), 125106.

Beall, J.M., Kim, Y.C. & Powers, E.J. 1982 Estimation of wavenumber and frequency spectra using fixed probe pairs. *J. Appl. Phys.* **53** (6), 3933–3940.

BENDAT, J.S. & PIERSOL, A.G. 2010 *Random Data: Analysis and Measurement Procedures*. John Wiley & Sons.

BRILLINGER, D.R. 2001 *Time Series: Data Analysis and Theory*. SIAM.

CHAUHAN, K., HUTCHINS, N., MONTY, J. & MARUSIC, I. 2013 Structure inclination angles in the convective atmospheric surface layer. *Boundary-Layer Meteorol.* **147** (1), 41–50.

CLIFF, W.C. & SANDBORN, V.A. 1973 Measurements and a model for convective velocities in the turbulent boundary layer. *NASA Tech. Rep.* TN D7416.

CUI, G. & JACOBI, I. 2023 Prediction of the phase difference between large-scale velocity and Reynolds stress fluctuations in wall turbulence. *J. Fluid Mech.* **969**, A13.

CUI, G., RUHMAN, I. & JACOBI, I. 2022 Spatial detection and hierarchy analysis of large-scale particle clusters in wall-bounded turbulence. *J. Fluid Mech.* **942**, A52.

DE KAT, R. & GANAPATHISUBRAMANI, B. 2015 Frequency-wavenumber mapping in turbulent shear flows. *J. Fluid Mech.* **783**, 166–190.

DEL ÁLAMO, J.C. & JIMÉNEZ, J. 2009 Estimation of turbulent convection velocities and corrections to Taylor's approximation. *J. Fluid Mech.* **640**, 5–26.

DEL ÁLAMO, J.C., JIMÉNEZ, J., ZANDONADE, P. & MOSER, R.D. 2004 Scaling of the energy spectra of turbulent channels. *J. Fluid Mech.* **500**, 135–144.

DENNIS, D.J.C. & NICKELS, T.B. 2008 On the limitations of Taylor's hypothesis in constructing long structures in a turbulent boundary layer. *J. Fluid Mech.* **614**, 197–206.

DESHPANDE, R., MONTY, J.P. & MARUSIC, I. 2019 Streamwise inclination angle of large wall-attached structures in turbulent boundary layers. *J. Fluid Mech.* **877**, 1–13.

ELSINGA, G.E., POELMA, C., SCHRÃDER, A., GEISLER, R., SCARANO, F. & WESTERWEEL, J. 2012 Tracking of vortices in a turbulent boundary layer. *J. Fluid Mech.* **697**, 273–295.

FERNHOLZ, H.H. & FINLEY, P.J. 1996 The incompressible zero-pressure-gradient turbulent boundary layer: an assessment of the data. *Prog. Aerosp. Sci.* **32** (4), 245–311.

FISHER, N.I. 1995 *Statistical Analysis of Circular Data*. Cambridge University Press.

FLORES, O. & JIMENEZ, J. 2006 Effect of wall-boundary disturbances on turbulent channel flows. *J. Fluid Mech.* **566**, 357–376.

FOUCAUT, J., CARLIER, J. & STANISLAS, M. 2004 PIV optimization for the study of turbulent flow using spectral analysis. *Meas. Sci. Technol.* **15** (6), 1046.

GAN, L., DAWSON, J.R. & NICKELS, T.B. 2012 On the drag of turbulent vortex rings. *J. Fluid Mech.* **709**, 85–105.

GENG, C., HE, G., WANG, Y., XU, C., LOZANO-DURÁN, A. & WALLACE, J.M. 2015 Taylor's hypothesis in turbulent channel flow considered using a transport equation analysis. *Phys. Fluids* **27** (2), 025111.

HE, G., JIN, G. & YANG, Y. 2017 Space–time correlations and dynamic coupling in turbulent flows. *Annu. Rev. Fluid Mech.* **49**, 51–70.

HE, G. & ZHANG, J. 2006 Elliptic model for space–time correlations in turbulent shear flows. *Phys. Rev.* E **73** (5), 2–5.

HOYAS, S. & JIMÉNEZ, J. 2006 Scaling of the velocity fluctuations in turbulent channels up to $Re_\tau = 2003$. *Phys. Fluids* **18** (1), 011702.

HUANG, H. 2019 Refining the connection between the logarithmic velocity profile and energy spectrum based on eddy's inclination angle. *Phys. Rev. Fluids* **4** (11), 1–10.

HUTCHINS, N. & MARUSIC, I. 2007 Large-scale influences in near-wall turbulence. *Phil. Trans. R. Soc.* A **365** (1852), 647–664.

JACOBI, I. & MCKEON, B.J. 2013 Phase relationships between large and small scales in the turbulent boundary layer. *Exp. Fluids* **54** (3), 1481.

JIMÉNEZ, J., DEL ALAMO, J.C. & FLORES, O. 2004 The large-scale dynamics of near-wall turbulence. *J. Fluid Mech.* **505**, 179–199.

KEISLER, S.R. 1976 An assessment of prewhitening in estimating power spectra of atmospheric turbulence at long wavelengths. *NASA Tech. Rep.* TN D8288.

KIM, J. & HUSSAIN, F. 1992 Propagation velocity of perturbations in turbulent channel flow. *Phys. Fluids* A **5** (3), 695–706.

KIM, K.C. & ADRIAN, R.J. 1999 Very large-scale motion in the outer layer. *Phys. Fluids* **11** (2), 417–422.

KRAICHNAN, R.H. 1964 Kolmogorov's hypotheses and Eulerian turbulence theory. *Phys. Fluids* **7** (11), 1723–1734.

LEE, M. & MOSER, R.D. 2015 Direct numerical simulation of turbulent channel flow up to. *J. Fluid Mech.* **774**, 395–415.

LEHEW, J.A. 2012 Spatio-temporal analysis of the turbulent boundary layer and an investigation of the effects of periodic disturbances. PhD thesis, California Institute of Technology.

LeHew, J.A., Guala, M. & McKeon, B.J. 2011 A study of the three-dimensional spectral energy distribution in a zero pressure gradient turbulent boundary layer. *Exp. Fluids* **51** (4), 997–1012.

LeHew, J.A., Guala, M. & McKeon, B.J. 2013 Time-resolved measurements of coherent structures in the turbulent boundary layer. *Exp. Fluids* **54** (4), 1508.

Li, X., Hutchins, N., Zheng, X., Marusic, I. & Baars, W.J. 2022 Scale-dependent inclination angle of turbulent structures in stratified atmospheric surface layers. *J. Fluid Mech.* **942**, 1–16.

Lin, C.C. 1953 On Taylor's hypothesis and the acceleration terms in the Navier–Stokes equations. *Q. Appl. Maths* **10** (4), 295–306.

Liu, C. & Gayme, D.F. 2020 An input–output based analysis of convective velocity in turbulent channels. *J. Fluid Mech.* **888**, A32.

Lozano-Durán, A. & Jiménez, J. 2014 Time-resolved evolution of coherent structures in turbulent channels: characterization of eddies and cascades. *J. Fluid Mech.* **759**, 432–471.

Lumley, J.L. 1965 Interpretation of time spectra measured in high-intensity shear flows. *Phys. Fluids* **8** (6), 1056–1062.

Marusic, I., Monty, J.P., Hultmark, M. & Smits, A.J. 2013 On the logarithmic region in wall turbulence. *J. Fluid Mech.* **716** (1976), 1–11.

McKeon, B.J. 2017 The engine behind (wall) turbulence: perspectives on scale interactions. *J. Fluid Mech.* **817**, 1–86.

Narita, Y. 2017 Spectral moments for the analysis of frequency shift, broadening, and wavevector anisotropy in a turbulent flow. 3. Space science. *Earth Planet. Space* **69**, 73.

Natrajan, V.K., Wu, Y. & Christensen, K.T. 2007 Spatial signatures of retrograde spanwise vortices in wall turbulence. *J. Fluid Mech.* **574**, 155–167.

Nikias, C.L. & Raghuveer, M.R. 1987 Bispectrum estimation: a digital signal processing framework. *Proc. IEEE* **75** (7), 869–891.

Otnes, R.K. 1978 *Applied Time Series Analysis*. Wiley-Interscience.

Oxlade, A.R., Valente, P.C., Ganapathisubramani, B. & Morrison, J.F. 2012 Denoising of time-resolved PIV for accurate measurement of turbulence spectra and reduced error in derivatives. *Exp. Fluids* **53** (5), 1561–1575.

Perry, A.E., Henbest, S. & Chong, M.S. 1986 A theoretical and experimental study of wall turbulence. *J. Fluid Mech.* **165**, 163–199.

Renard, N. & Deck, S. 2015 On the scale-dependent turbulent convection velocity in a spatially developing flat plate turbulent boundary layer at Reynolds number $Re_\theta = 13\,000$. *J. Fluid Mech.* **775**, 105–148.

Saunders, K.D. & Hamrick, F.C. 1982 A note on cross spectrum and coherence calculations. *J. Geophys. Res.* **87** (C12), 9699–9703.

Wilczek, M. & Narita, Y. 2012 Wave-number-frequency spectrum for turbulence from a random sweeping hypothesis with mean flow. *Phys. Rev.* E **86** (6), 1–8.

Wilczek, M., Stevens, R.J.A.M. & Meneveau, C. 2015*a* Height-dependence of spatio-temporal spectra of wall-bounded turbulence – LES results and model predictions. *J. Turbul.* **16** (10), 937–949.

Wilczek, M., Stevens, R.J.A.M. & Meneveau, C. 2015*b* Spatio-temporal spectra in the logarithmic layer of wall turbulence: large-eddy simulations and simple models. *J. Fluid Mech.* **769**, 1–12.

Wilczek, M., Stevens, R.J.A.M., Narita, Y. & Meneveau, C. 2014 A wavenumber-frequency spectral model for atmospheric boundary layers. *J. Phys.: Conf. Ser.* **524** (1), 1–6.

Wu, T., Geng, C., Yao, Y., Xu, C. & He, G. 2017 Characteristics of space–time energy spectra in turbulent channel flows. *Phys. Rev. Fluids* **2** (8), 1–11.

Wu, T. & He, G. 2021*a* Space–time energy spectra in turbulent shear flows. *Phys. Rev. Fluids* **6** (10), 1–23.

Wu, T. & He, G. 2021*b* Stochastic dynamical model for space–time energy spectra in turbulent shear flows. *Phys. Rev. Fluids* **6** (5), 1–23.

Yang, B., Jin, G., Wu, T., Yang, Z. & He, G. 2020 Numerical implementation and evaluation of resolvent-based estimation for space–time energy spectra in turbulent channel flows. *Acta Mechanica Sin.* **36** (4), 775–788.